

















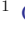



Rotational Evolution of Classical T Tauri Stars: Models and Observations*

JAVIER SERNA ¹, GIOVANNI PINZÓN ², JESÚS HERNÁNDEZ ¹, EZEQUIEL MANZO-MARTÍNEZ ¹, KARINA MAUCO ^{1,3},
CARLOS G. ROMÁN-ZÚÑIGA ¹, NURIA CALVET ⁴, CESAR BRICEÑO ⁵, RICARDO LÓPEZ-VALDIVIA ¹,
MARINA KOUNKEL ⁶, GUY S. STRINGFELLOW ⁷, KEIVAN G. STASSUN ⁶, MARC PINSONNEALT ⁸, LUCIA ADAME ¹,
LYRA CAO ⁸, KEVIN COVEY ⁹, AMELIA BAYO ^{10,3}, ALEXANDRE ROMAN-LOPES ¹¹, CHRISTIAN NITSCHHELM ¹² AND
RICHARD R. LANE ¹³

¹*Instituto de Astronomía, Universidad Autónoma de México, Ensenada, B.C, México*

²*Observatorio Astronómico Nacional, Universidad Nacional de Colombia, Bogotá, Colombia*

³*European Southern Observatory, Karl-Schwarzschild-Strasse 2, 85748 Garching bei München, Germany*

⁴*Department of Astronomy, University of Michigan, 1085 South University Avenue, Ann Arbor, MI 48109, USA*

⁵*Cerro Tololo Inter-American Observatory/NSF's NOIRLab, Casilla 603, La Serena, Chile*

⁶*Department of Physics and Astronomy, Vanderbilt University, VU Station 1807, Nashville, TN 37235, USA*

⁷*Center for Astrophysics and Space Astronomy, Department of Astrophysical and Planetary Sciences, University of Colorado, Boulder, CO, 80309, USA*

⁸*Department of Astronomy, The Ohio State University, Columbus, OH 43210, USA*

⁹*Department of Physics and Astronomy, Western Washington University, 516 High St, Bellingham, WA 98225*

¹⁰*Instituto de Física y Astronomía, Universidad de Valparaíso, Chile*

¹¹*Departamento de Astronomía, Universidad de La Serena, 1700000 La Serena, Chile*

¹²*Centro de Astronomía (CITEVA), Universidad de Antofagasta, Avenida Angamos 601, Antofagasta 1270300, Chile*

¹³*Centro de Investigación en Astronomía, Universidad Bernardo O'Higgins, Avenida Viel 1497, Santiago, Chile*

(Accepted in ApJ, March 13, 2024)

ABSTRACT

We developed a grid of stellar rotation models for low-mass and solar-type Classical T Tauri stars (CTTS) ($0.3M_{\odot} < M_{*} < 1.2M_{\odot}$). These models incorporate the star-disk interaction and magnetospheric ejections to investigate the evolution of the stellar rotation rate as a function of the mass of the star M_{*} , the magnetic field (B_{*}), and stellar wind (\dot{M}_{wind}). We compiled and determined stellar parameters for 208 CTTS, such as projected rotational velocity $v \sin(i)$, mass accretion rate \dot{M}_{acc} , stellar mass M_{*} , ages, and estimated rotational periods using TESS data. We also estimated a representative value of the mass-loss rate for our sample using the [O I] $\lambda 6300$ spectral line. Our results confirm that $v \sin(i)$ measurements in CTTS agree with the rotation rates provided by our spin models in the accretion-powered stellar winds (APSW) picture. In addition, we used the Approximate Bayesian Computation (ABC) technique to explore the connection between the model parameters and the observational properties of CTTS. We find that the evolution of $v \sin(i)$ with age might be regulated by variations in (1) the intensity of B_{*} and (2) the fraction of the accretion flow ejected in magnetic winds, removing angular momentum from these systems. The youngest stars in our sample (~ 1 Myr) show a median branching ratio $\dot{M}_{wind}/\dot{M}_{acc} \sim 0.16$ and median $B_{*} \sim 2000$ G, in contrast to ~ 0.01 and 1000 G, respectively, for stars with ages $\gtrsim 3$ Myr.

Keywords: Classical T Tauri stars (252) – Stellar evolution (1599) – Stellar magnetic fields (1610) – Stellar properties (1624) – Stellar rotation (1629) – Stellar winds (1636)

Corresponding author: Javier Serna
jserna@astro.unam.mx

* March 13, 2024

1. INTRODUCTION

Low mass ($< 1.2M_{\odot}$), Classical T Tauri Stars (CTTS) are young systems, still contracting and accreting gas

from their circumstellar disks through the stellar magnetic field. Despite crossing a phase of gravitational contraction, the rotation rates of the majority of CTTS lie well below 10% of their break-up limit (Bouvier et al. 1993, Herbst et al. 2002, Jayawardhana et al. 2006, Nguyen et al. 2009, Bayo et al. 2012, Pinzón et al. 2021, Serna et al. 2021), indicating that these stars lose angular momentum expeditiously during the first million years (Myr).

In the so-called Disk-Locking (DL) scenario, angular momentum in CTTS is transferred outward from the star to the disk regions beyond the corotation radius through the stellar magnetic field closed lines anchored to the star surface (Ghosh & Lamb 1979, Collier Cameron & Campbell 1993a). Nevertheless, the stellar spin-down efficiency in the DL model is substantially reduced due to the turbulent diffusion of the field inside the disk, which results in more realistic magnetic field topologies with open field regions (Matt & Pudritz 2005a). These regions allow the appearance of stellar winds, which are an alternative source of angular momentum loss (Matt & Pudritz 2008a).

CTTS exhibit energetic stellar and disk winds traced through the blue-shifted absorption profiles of their most prominent lines and by the presence of intense forbidden line emission of low ionization species in their spectra (Kuhi 1964, Hartmann et al. 1982, Alencar & Basri 2000, Edwards et al. 2003). The correlation between the forbidden line emission and stellar accretion suggests that such winds are somehow powered by disk accretion (Hartigan et al. 1995). However, how the energy is transferred from the accretion flow to a stellar wind through the corona is still unknown.

Magnetohydrodynamic (MHD) simulations of CTTS, including stellar and disk wind scenarios, have shown that stellar rotation can reach an equilibrium around 10% of the break-up limit at the end of the Hayashi track for X-wind models (Shu et al. 1988). Mass loss mechanisms such as stellar wind models (Tout & Pringle 1992), accretion-powered stellar winds models (APSW, Matt & Pudritz 2008a,b), and disk wind models (Zanni & Ferreira 2013, Ercolano et al. 2021) can be involved to reach this equilibrium. While all these models rely on the basis that a fraction of the accretion luminosity powers the stellar wind, only APSW establishes an upper limit for the so-called branching ratio between the mass loss rate in the stellar wind and the disk accretion rate ($\chi \equiv \dot{M}_{wind}/\dot{M}_{acc}$). This upper limit of $\chi \sim 0.6$ has been confirmed by Watson et al. (2016) using infrared

forbidden line emission from the Spitzer and Herschel observations. The authors obtain a distribution of χ centered close to 0.1 with a tail towards lower values ($\chi < 0.6$), whose effect on the angular momentum evolution of CTTS has not been properly explored.

In this work, we computed synthetic rotational velocities for low-mass stars ($0.3M_{\odot} < M_{*} < 1.2M_{\odot}$) in the framework of APSW models with the aim of obtaining the branching ratio distribution of a well-characterized CTTS sample with available rotation rates and accretion indicators. We use a Bayesian approach to investigate the connection between the branching-ratio parameter, the stellar magnetic fields, rotational evolution, and internal structure. This paper is organized as follows. In §2, we describe the observations and data sources used to study our sample of CTTS. In §3, we estimate the rotation periods using the TESS light curves. We derive the stellar mass accretion rate based on the H_{α} spectral line and identify wind tracers (e.g., [O I] $\lambda 6300$) to estimate the mass-loss rate by winds (\dot{M}_{wind}). We also build and present the spin models for CTTS and use the Approximate Bayesian Computation (ABC) technique to investigate the connection between the model parameters and available observable distributions of CTTS. In §4, we discuss the implications of our results. Finally, in §5, we present the conclusions of this work.

2. T TAURI STARS SAMPLE AND DATA SOURCES

2.1. CTTS Sample

We use the sub-sample of 208 CTTS studied in Serna et al. (2021). This sub-sample has been confirmed and characterized by Briceño et al. (2019) and Hernández et al. (2014). It includes low-mass accretors of the on/off cloud population in the Orion OB1 association, which span ages from 1 to 10 Myr (e.g., ONC, σ Ori, 25 Ori). Each of these targets has measurements of the H_{α} equivalent width, $v \sin(i)$, as well as masses and ages derived using the **MassAge** code (Serna et al. 2021, Hernández et al., in preparation). The list of parameters can be seen in Table 1.

2.2. APOGEE-2 Data and Stellar Parameters

The APOGEE-2 northern spectrograph (APOGEE; Majewski et al. 2017) is located on the 2.5 m SDSS telescope at the Apache Point Observatory and observed thousands of stars for the APOGEE-2 Young Cluster Survey. This instrument can simultaneously observe up to 300 objects at high resolution ($R \sim 22500$) in the

H-band (15100–17000Å) across a 1.5 deg radius field-of-view.

Kounkel et al. (2018) analyzed data from the APOGEE-2 survey in the Orion Star-Forming Complex and reported nearly 2400 kinematic members using six-dimensional analysis (positions, parallax, and proper motions from *Gaia*-DR2 and radial velocities (RV) from APOGEE-2). Additionally, for each one of these members, Kounkel et al. (2019) report (effective temperature T_{eff} , surface gravity $\log(g)$, $v \sin(i)$, RV). However, the authors warn that there are likely systematic features in the parameter space due to theoretical templates not offering a perfect match to the real data. To reduce these issues on the estimated parameters, Olney et al. (2020), based on a deep learning analysis, have provided more reliable predictions of $\log g$, T_{eff} , and [Fe/H] for low-mass stars. More recently, Serna et al. (2021) estimated $v \sin(i)$ using the Fourier method, an independent method that does not require theoretical templates, and found that measurements are in agreement with the estimations of Kounkel et al. (2019), indicating that the systematic features in the parameter space suggested by these authors do not affect their $v \sin(i)$ derivation. Since the Fourier method requires a high signal-to-noise ratio, applying this method to the entire CTTS sample was not possible. Thus, we adopt Kounkel et al. (2019) measurements for our sample of CTTS.

2.3. LAMOST

We use the data archive from the Large Sky Area Multi-Object Fiber Spectroscopic Telescope (LAMOST; Luo et al. 2015, Liu et al. 2020), located on the 4-meter quasi-meridian reflecting Schmidt telescope at the Xinlong station of the National Astronomical Observatory. We downloaded 55 spectra of our CTTS sample at low-resolution ($R \sim 1800$) in the wavelength range 3650–9000Å, and 7 spectra at medium-resolution ($R \sim 7500$) in two bands, which cover the wavelength ranges 4950–5350Å, and 6300–6800Å. From these spectra, only 24 have the presence of the [O I] $\lambda 6300$ line, which was used for the mass-loss rate estimations §3.1.3. The remaining spectra of the 55 stars without [OI] were not used in the analysis. The details of the LAMOST data and plots of the [O I] $\lambda 6300$ profile are presented in Appendix A.

2.4. X-Shooter and Giraffe/ESO

We download spectra for 25 CTTS using the ESO Archive Science Portal. From this sample, there are

15 stars with resolution $R < 18340$ (X-Shooter) and 10 stars with $R = 24000$ (Giraffe); both instruments are installed in the ESO Very Large Telescope (Vernet et al. 2011). We rejected three stars observed with Giraffe that do not exhibit the [O I] $\lambda 6300$ line. We use the data reduced and flux-calibrated by the ESO calibration pipelines available in the ESO archive. Additionally, we used the *Molecfit* tool (Kausch et al. 2015) to correct each spectrum from telluric lines. Table 2 shows a summary and observations details.

Table 1. Stellar parameters of the CTTS sample

2MASS ID	$v \sin(i)^a$ (km s ⁻¹)	M_* (M_\odot)	Age (Myr)	P_{rot}^b (days)	P_{rot}^c (days)	$\log \dot{M}_{acc}$ ($\log M_\odot \text{ yr}^{-1}$)	$\log \dot{M}_{wind}$ ($\log M_\odot \text{ yr}^{-1}$)	Binary ^a
(1)	(2)	(3)	(4)	(5)	(6)	(7)	(8)	(9)
05390878-0231115	12.8 ± 0.6	0.3 ± 0.03	2.36 ± 0.53	-9.37 ± 0.31	-11.13 ± 0.83	1
05380097-0226079	16.2 ± 0.5	0.37 ± 0.03	3.77 ± 0.85	-9.01 ± 0.3	-10.43 ± 0.84	1
05344178-0453462	10.7 ± 0.7	0.44 ± 0.04	1.73 ± 0.33	-8.95 ± 0.3	-10.05 ± 0.84	1
05373094-0223427	7.7 ± 0.6	0.36 ± 0.03	6.66 ± 1.46	-8.93 ± 0.3	-10.38 ± 0.84	1
05391151-0231065	13.7 ± 0.5	0.5 ± 0.04	1.3 ± 0.21	-8.89 ± 0.3	-9.76 ± 0.84	1
05332852-0517262	8.1 ± 1.2	0.5 ± 0.04	1.56 ± 0.27	-8.7 ± 0.29	-10.26 ± 0.83	1
05380826-0235562	8.8 ± 0.5	0.4 ± 0.03	1.03 ± 0.18	-8.68 ± 0.29	-9.9 ± 0.84	1
05384027-0230185	18.3 ± 1.1	0.49 ± 0.03	0.8 ± 0.11	7.69 ± 0.01	...	-8.67 ± 0.29	-9.37 ± 0.85	1
05402461-0152309	14.4 ± 0.5	0.54 ± 0.04	1.9 ± 0.34	-8.66 ± 0.29	-10.02 ± 0.84	1
05393938-0217045	14.1 ± 0.5	0.6 ± 0.04	0.98 ± 0.16	...	13.52 ± 0.01	-8.61 ± 0.29	-9.93 ± 0.83	1
05343395-0534512	22.3 ± 0.5	0.54 ± 0.04	0.82 ± 0.12	-8.56 ± 0.29	-9.03 ± 0.85	1
05395362-0233426	0.1 ± 0.6	0.35 ± 0.03	2.68 ± 0.55	-8.56 ± 0.29	-10.75 ± 0.83	1
05324196-0539239	60.7 ± 1.7	0.75 ± 0.07	0.41 ± 0.07	1.7 ± 0.01	1.69 ± 0.01	-8.56 ± 0.29	-9.29 ± 0.84	-1
05400195-0221325	8.8 ± 0.5	0.36 ± 0.03	0.96 ± 0.15	-8.54 ± 0.28	-10.71 ± 0.83	1
05391883-0230531	47.9 ± 2.6	1.1 ± 0.18	2.45 ± 1.33	...	1.83 ± 0.01	-8.53 ± 0.28	-9.79 ± 0.83	-1
05380674-0230227	15.3 ± 2.1	0.52 ± 0.03	0.77 ± 0.11	-8.51 ± 0.28	-9.05 ± 0.85	1
05401274-0228199	50.9 ± 1.4	0.45 ± 0.03	0.52 ± 0.05	1.53 ± 0.01	...	-8.49 ± 0.28	-10.86 ± 0.81	-1
05354600-0057522	10.3 ± 0.7	0.65 ± 0.05	1.75 ± 0.32	-8.49 ± 0.28	-10.01 ± 0.83	1*
05341420-0542210	5.4 ± 1.1	0.62 ± 0.05	2.53 ± 0.52	-8.42 ± 0.28	-9.12 ± 0.85	1
05394017-0220480	16.1 ± 0.8	0.77 ± 0.05	1.6 ± 0.27	5.8 ± 0.01	5.64 ± 0.01	-8.4 ± 0.28	-9.73 ± 0.84	1

^aKounkel et al. (2018), Kounkel et al. (2019): 0- Undeconvolvable cross-correlation function (CCF); 1- Only a single component in the CCF; 2- Multiple components in the CCF; -1- Spotted pairs or SB2 Uncertain

^bTESS Sector 6

^cTESS Sector 32

* Tokovinin et al. (2020) visual binaries

NOTE—Only a portion of the table is shown here. The full version is available in electronic form.

2.5. TESS Data

From the initial sample of 208 CTTS, we have 194 stars observed by TESS at 10 min and 30 min cadences for at least ~ 25 days. We build each light curve (LC) using the `TESSExtractor`¹ application (Serna et al. 2021), which uses simple aperture photometry (SAP) to extract the stellar fluxes from the Full-frame images (FFI) provided by TESScut (Brasseur et al. 2019). Also, we use the Cotrending basis vectors (CBVs) from TESS and the task `kepcotrend` of the PyKE package (Still & Barclay 2012) to correct the LCs from any systematic effect on the data. Once LCs were adequately processed, we performed a visual inspection and flagged the sources that exhibited periodic or quasi-periodic events as candidates for their posterior period analysis. Figure 1 shows an example of the graphical product generated by the `TESSExtractor` application. This product includes the light curve, the phase-folded curve, and the periodogram used to obtain rotational periods. For more details, see section 3.1.1.

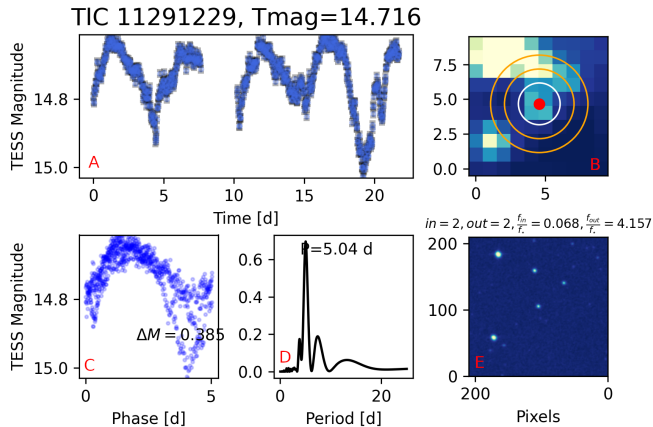


Figure 1. TESS light curve and analysis for the target TIC 11291229. *Top:* (A) Light curve in TESS magnitudes, the error bars are contained in the marker symbols. The label on top refers to the star identification and the mean TESS magnitude. (B) Field of view (210 x 210 sq arcsec) corresponding to a TESS image of 10x10 pixels. The white circle shows the photometric aperture, and the orange circle shows the sky annulus. The red dot marks the centroid of the star. *Bottom:* (C) Phase-folded light curve to the estimated best period. The legend shows the amplitude. (D) Lomb-Scargle periodogram, with the estimated period. (E) 210 x 210 pixels Digital Sky Survey (DSS2) thumbnail, same field of view as (B).

3. ANALYSIS AND RESULTS

3.1. Stellar Parameters

3.1.1. Rotation Period

Several variability studies in young stellar objects (YSOs) have revealed that most CTTS exhibit complex flux variations on timescales of hours, days, and even years (Bouvier et al. 1993, Cody & Hillenbrand 2010, Roggero et al. 2021). In some cases, brightness fluctuations are observed at levels of 1% to 10%, with fading or brightening events and quasi-periodic structures in most instances (Cody et al. 2014). It has been proposed that these flux variations are generated by various mechanisms, such as the rotation of hot and cold starspots, accretion bursts (e.g., Espaillat et al. 2021), occultations by dusty disk structures (e.g., Ansdell et al. 2019), and accretion streams falling at random locations on the star (Kurosawa & Romanova 2013). These processes may be acting at once in CTTS, challenging the estimations of P_{rot} for most stars. However, according to the DL model, the magnetic connection between the star and its inner disk results in synchronization between the stellar angular velocity and the Keplerian velocity at the corotation radius (Artemenko et al. 2012), particularly for the first 3 Myr of the CTTS evolution (Matt et al. 2010, 2012). Then, assuming a Keplerian rotation regime, any periodic signal produced at the corotation zone could proxy the stellar rotation at the stellar surface. Therefore, under this assumption, we have estimated rotation periods for those candidates that show an apparent periodicity in the TESS data (§2.5).

From the sample of LCs in §2.5, only 51 stars exhibit periodic behavior to study rotation. We have selected light curves with a false alarm probability (FAP) below 0.01%, indicating that the period measurements are highly reliable. We use the task `statistics.false_alarm_probability` from the `astropy` package (Astropy Collaboration et al. 2013). We use the Lomb-Scargle periodogram (Lomb 1976, Scargle 1982) to estimate the rotational period from the LC. We use a resolution of 1000 steps within the interval $0.01 < P < 25$ days. The best period was selected as the highest peak in the periodogram (see lower middle panel of Figure 1). These periods have been confirmed by checking the periodic pattern using the phase-folded LC at the estimated period, as shown in Figure 1. The P_{rot} are listed in Table 1. We plot the histogram of the periods in Figure 2. The range of periods estimated in this section will be used as input in the models §3.2.1, see Table 3.

¹ <https://www.tessexttractor.app>

Table 2. Summary of ESO archival spectroscopy

Target	Instrument [*]	Spectral Resolution	Obs. Date (UT)	Exp. time (s)	SNR	ESO Program ID
SO 73	XSHOOTER	8935	2019-11-18	2400	106	0104.C-0454(A)
SO 299	GIRAFFE	24000	2009-02-04	2775	22	082.C-0313(B)
SO 341	XSHOOTER	1029	2020-02-07	90	28	0104.C-0454(A)
SO 362	XSHOOTER	1512	2020-02-07	200	41	0104.C-0454(A)
SO 662	XSHOOTER	1512	2020-02-07	60	38	0104.C-0454(A)
SO 908	GIRAFFE	24000	2010-01-03	2775	39	084.C-0282(A)
SO 927	GIRAFFE	24000	2010-01-03	2775	62	0103.C-0887(B)
SO 984	XSHOOTER	18340	2019-11-17	420	83	0104.C-0454(A)
SO 1036	XSHOOTER	1512	2019-10-11	60	37	0104.C-0454(A)
SO 1075	GIRAFFE	24000	2010-01-03	2775	26	084.C-0282(A)
SO 1152	XSHOOTER	18340	2019-10-12	800	73	0104.C-0454(A)
SO 1153	XSHOOTER	1512	2021-02-13	60	37	106.20Z8.002
SO 1156	XSHOOTER	1512	2019-10-28	60	44	0104.C-0454(A)
SO 1260	GIRAFFE	24000	2010-01-03	2775	40	084.C-0282(A)
SO 1267	XSHOOTER	1512	2019-11-17	60	33	0104.C-0454(A)
SO 1327	GIRAFFE	24000	2010-01-03	2775	33	084.C-0282(A)
SO 1368	GIRAFFE	24000	2010-01-03	2775	79	0103.C-0887(B)
SO 1361	XSHOOTER	1512	2019-12-09	60	40	0104.C-0454(A)
CVSO 58	XSHOOTER	1512	2020-12-02	65	27	106.20Z8.002
CVSO 90	XSHOOTER	18340	2020-12-04	740	80	106.20Z8.002
CVSO 107	XSHOOTER	18340	2020-12-04	740	80	106.20Z8.002
CVSO 146	XSHOOTER	1512	2020-12-09	40	42	106.20Z8.002
CVSO 1876	GIRAFFE	24000	2010-01-03	2775	72	084.C-0282(A)
CVSO 1885	GIRAFFE	24000	2010-01-03	2775	49	084.C-0282(A)
V605 Ori B	GIRAFFE	24000	2010-01-03	2775	39	084.C-0282(A)

^{*}The spectral coverage for the X-Shooter data 533.7-1020 nm and Giraffe 611.38-640.37 nm.

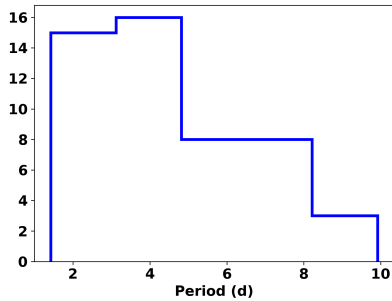


Figure 2. Rotational periods for the CTTS sample obtained through TESS light-curve analysis. The bin size used in the histogram follows Scott’s rule (Scott 1979).

3.1.2. Mass Accretion Rate

We determined mass accretion rates for the 208 stars of the sample in §2.1 based on the $H\alpha$ equivalent width ($EW_{H\alpha}$), spectral types, and reddening A_V reported by Briceño et al. (2019), Hernández et al. (2014, Hernández et al., in preparation). Also, we use the *Gaia* DR3 parallax measurements corrected by systematics and the *Gaia* G , G_{BP} , and G_{RP} photometry (Gaia Collaboration et al. 2022, Lindegren et al. 2021). Using the relationship between the Johnson-Cousins photometric system and the *Gaia* photometry², we obtain the V magnitude. Given the spectral type and using the V magnitude corrected by extinction, the $I_{c,0}$ magnitude is obtained from the intrinsic $[V - I_c]_0$ color from Pecaut &

² from Table 5.8 of the *Gaia* data release 2 documentation <https://gea.esac.esa.int/archive/documentation/GDR2/>

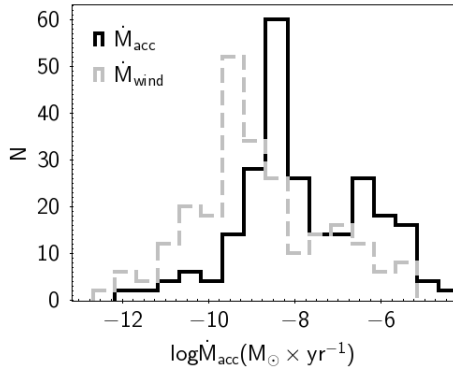


Figure 3. Mass accretion and mass loss rates for the sample of CTTS.

Mamajek (2013). To obtain the continuum flux at the $H\alpha$ line (F_{cont}), we estimate the fluxes at the $V(0.55 \mu m)$ and $I_c(0.79 \mu m)$ bands and interpolate the flux at $0.6563 \mu m$. Using the $H\alpha$ equivalent width and distance estimated by the inverse relation with the parallax, we estimate the luminosity of the $H\alpha$ as follows:

$$L_{H\alpha} = 4\pi d^2 \times (EWH_{\alpha}) \times F_{cont} \quad (1)$$

Subsequently, we obtain the accretion luminosity using the following relation (Ingleby et al. 2013):

$$\log(L_{acc}) = 1.0(\pm 0.2) \log(L_{H\alpha}) + 1.3(\pm 0.7). \quad (2)$$

Finally, the mass accretion rate is obtained from $L_{acc} = GM_* \dot{M}_{acc} / R_*$, where M_* and R_* are determined using the MIST evolutionary models (Dotter 2016). The mass accretion rates distribution is shown in Figure 3, and corresponding values are included in Table 1.

3.1.3. Mass loss Rate Determination

We computed mass loss rates for a sub-sample of the CTTS described in §2.1 via the forbidden emission line of [O I] $\lambda 6300$, which has been widely used as a tracer of bi-polar jets, stellar and disk winds (e.g., Cabrit et al. 1990, Edwards et al. 2003, Watson et al. 2016, Pascucci et al. 2022). Specifically, we compute mass loss rates for 24 CTTS with LAMOST spectra (§2.3), 15 CTTS with X-Shooter spectra, and 7 CTTS with Giraffe spectra (§2.4). Luminosities of [OI] emission lines are computed from equivalent widths and dereddened fluxes at wavelengths near 6300 \AA and used as indicators of the amount of mass in the outflow (Hartigan et al. 1995). Forbidden lines typically exhibit two components: a low-velocity component (LVC), which is symmetric and slightly blue-shifted, and a high-velocity component (HVC), with its peak either blue or red-shifted and separated from the LVC just a few tens of km s^{-1} (e.g., Hartigan et al.

1995, Natta et al. 2014, Simon et al. 2016, Banzatti et al. 2019).

Following the physical treatment to the mass-loss rate in the Appendix A1 of Hartigan et al. (1995) and references therein, we use the luminosity of the [O I] $\lambda 6300$, identified in the optical spectra of our CTTS to estimate the mass-loss rate ($\dot{M}_{wind} = MV_{\perp} / l_{\perp}$), where M is the mass in the flow whose dependence with the [O I] $\lambda 6300$ luminosity was taken from Hartigan et al. (1995), the V_{\perp} is the component of the velocity of the projected wind in the plane of the sky, and l_{\perp} corresponds to the size of the slit projected in the sky. In what follows, we assume $V_{\perp} = 150 \text{ km s}^{-1}$ as an average for all the stars (Hartigan et al. 1995), and based on the average distance to Orion ($d \sim 400 \text{ pc}$), we adopt $l_{\perp} = 6 \times 10^{15} \text{ cm}$ for X-shooter and Giraffe observations. For the case of the LAMOST spectra, the slit at the output end of the fibers is assumed to be equal to 2/3 of the fiber width leading to marginal differences relative to l_{\perp} . Thus, the correlation of Hartigan et al. (1995) may be written as follows:

$$\log_{10}(\dot{M}_{wind}) = -4.65 + \log_{10}\left(\frac{L_{\lambda 6300}}{L_{\odot}}\right) \quad (3)$$

Before analyzing any optical forbidden line profiles, we first remove any telluric and photospheric absorption contaminating the region of interest in the spectra. We used the Molecfit tool (Smette et al. 2015), which corrects for telluric absorption lines based on synthetic modeling of the Earth’s atmospheric transmission. To remove telluric lines, each spectrum was normalized and corrected by radial velocity (RV), using the RV reported in Kounkel et al. (2018), Hernández et al. (2014). Based on the effective temperature and $\log(g)$ of the star, we selected templates from the PHOENIX spectral library (Husser et al. 2013). In the specific case of the X-Shooter data, we use the XSL DR2 (Gonneau et al. 2020) to select a proper template for each star. Once spectra were corrected by RV, all the templates were broadened by their reported $v \sin(i)$ using the rotational kernel implemented in the PyAstronomy package (Czesla et al. 2019). Then, the broadened templates were subtracted from each observed spectrum.

In Figures 4, and 5 we show the line profiles. In order to get the luminosity of the line [O I] $\lambda 6300$ ($L_{\lambda 6300}$), we have used the distances of Gaia DR3, the equivalent width of [O I] $\lambda 6300$ ($EW[\text{OI}]$) obtained with the task *splot* of IRAF, a continuum flux estimation around the [O I] $\lambda 6300$, and the equation (1). In particular, for LAMOST and Giraffe spectra, the flux at the con-

tinuum was estimated interpolating two bands around 6300\AA as described in section 3.1.2. For the X-shooter spectra, we directly measure the flux because the spectra have been properly flux calibrated. Subsequently, using the equation (3), we estimate the mass-loss rate \dot{M}_{wind} of our sample and their uncertainty following the error propagation procedure.

This analysis remains valid as long as we have the presence of HVC in the [O I] $\lambda 6300$ line profiles. In some cases, our spectral resolution is insufficient to distinguish the HVC. We warn the reader to be cautious with results because the mass-loss rates for some sources could be overestimated. However, our results provide a helpful statistical estimation of the mass loss rate for this study. We summarize our results in Table 1.

Using the mass accretion rates estimated in §3.1.2 and the mass-loss rates of our sample, we roughly estimate the branching ratio χ of these systems. We plot in Figure 6 the accretion and mass-loss rates for our sample compared to other estimations of CTTS in the literature. Considering the limited mass and age intervals covered by our sample, accretion rate values range between $10^{-9} - 10^{-8} M_{\odot} yr^{-1}$ and mass-loss rates between $10^{-10} - 10^{-8} M_{\odot} yr^{-1}$ as shown in Figure 3. To have a more comprehensive view of a diverse population of CTTS, we included reported measurements for CTTS in Taurus (Herczeg & Hillenbrand 2008), Lupus (Natta et al. 2014), active CTTS systems from Hartigan et al. (1995), Gullbring et al. (1998), and CTTS in nine molecular cloud complexes studied by Watson et al. (2016) using Spitzer data. According to Figure 6, most of our CTTS remain below the APSW boundary (long-dashed black line), confirming that APSW is a suitable scenario to explain the observed rotation rates.

Although age information is not available in Figure 6, some studies have suggested evidence of temporal evolution between the \dot{M}_{acc} and \dot{M}_{wind} relationship. For instance, Watson et al. (2016) mostly includes objects younger than CTTS (e.g., Class 0 and Class I) and demonstrated that different classes of young objects, used as an age proxy, are naturally separated into different plot regions (see Figure 7 of Watson et al. 2016). Our study supports that evidence, providing more CTTS to the sample and showing even better how CTTS are well positioned in the plot.

3.1.4. Magnetic field topology and evolution

Observations indicate that the surface magnetic fields of young stars have high-order multipolar components rather than magnetic dipoles. While stars more massive than $0.5M_{\odot}$ exhibit toroidal and non-axisymmetric poloidal components, low-mass stars below $0.5M_{\odot}$ show strong poloidal large-scale magnetic fields, which are mainly axisymmetric (Donati & Landstreet 2009), where most CTTS have typical intensities of the order of 1-3 kG (Johns-Krull 2007), and significant star spot coverages (Somers et al. 2020, Cao & Pinsonneault 2022). These magnetic fields are expected to impact CTTS, their accretion disks, and planets (Strugarek et al. 2015).

Schatzman (1962) was the first to suggest that open magnetic field lines or the breaking of closed lines could trigger mass loss phenomena, which could, in the long run, be responsible for taking a large amount of angular momentum from the system. For this reason, the geometry of the magnetic field is an essential element in describing stellar winds. For example, Réville et al. (2015) and Garraffo et al. (2015) found that complexity in the geometry of the magnetic field can dramatically decrease the loss rate of angular momentum to a few orders of magnitude. This is mainly because higher orders of magnetic moments would facilitate the generation of a magnetosphere with many closed lines that would suppress mass loss. Emeriau-Viard & Brun (2017), Folsom et al. (2016) observed that the topology of the magnetic field changes strongly as the star ages because as the radiative core becomes bigger, the dipole components decrease, and the magnetic field becomes more and more complex. Folsom et al. (2016) and Vidotto et al. (2014) found empirical relationships between the large-scale component of the magnetic field strength versus age for pre-main to the main sequence.

Although there are many efforts to measure magnetic fields in T Tauri stars, nowadays, there is no conceptual model that allows us to describe magnetic fields accurately. Some authors approximate the magnetic field topologies, mixing different geometries. For example, Finley & Matt (2017) suggest that combinations of dipolar and quadrupolar fields change the relative orientation of the stellar wind with respect to any planetary or disk magnetic field. In a general view, these components are important in the morphology of the wind. Also, they confirm that the original prescription from Matt et al. (2012), which is the formulation of the present work, uses pure dipolar magnetic fields and remains robust in most cases, even for significantly

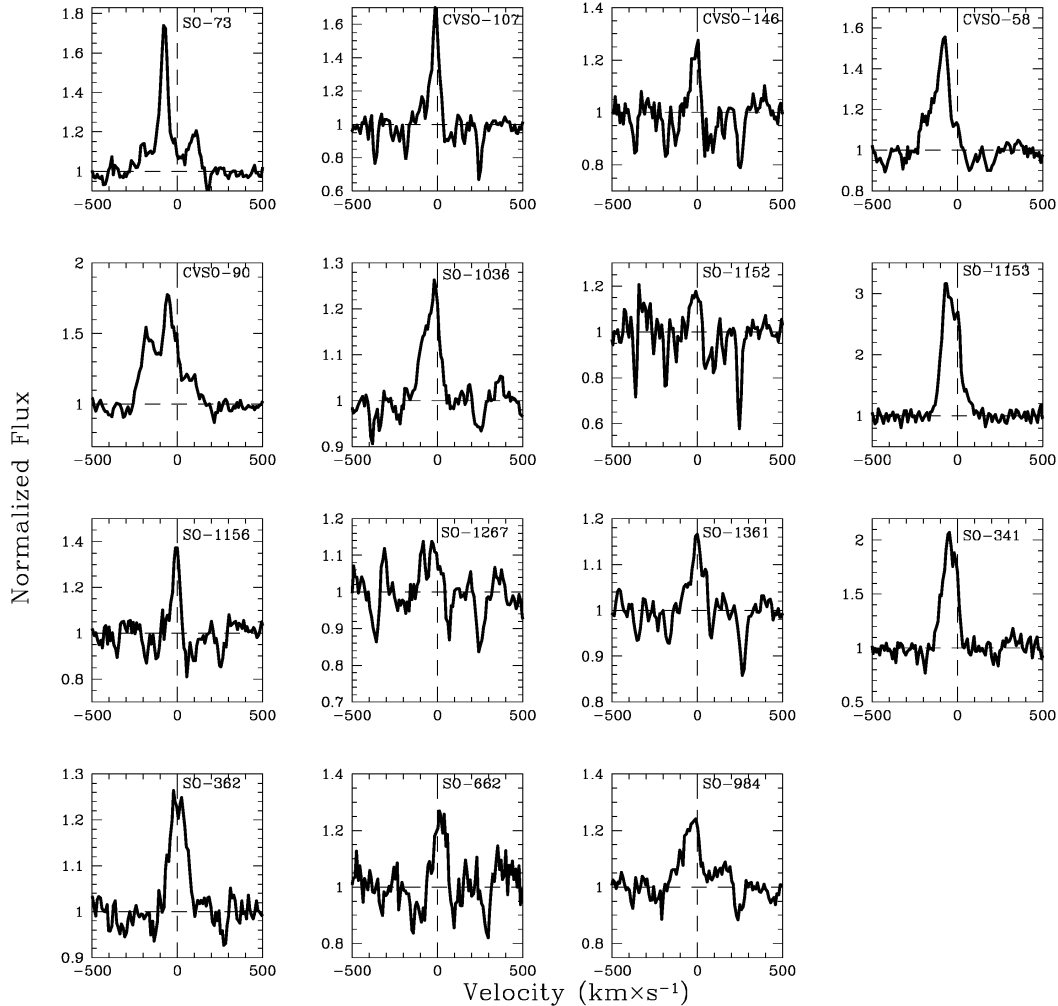


Figure 4. [O I] $\lambda 6300$ residual line profiles for 15 CTTS found in the X-Shooter data archive. The stellar rest velocity is indicated with a vertical dashed line. Residual emission lines were obtained by subtracting photospheric contributions using Phoenix templates and posterior removing telluric lines.

nondipolar fields.

3.2. Model Assumptions

We developed stellar spin multi-parametric models for young low-mass and solar-type stars magnetically linked to a surrounding gaseous accreting disk. We assume that stars can produce their stellar magnetic fields when they rotate, through dynamo processes in the convective regions of the stellar interior. Due to the size of the convective region varying with the spectral type, we use non-rotational, PMS evolutionary models of Baraffe et al. (2015) that provide a robust treatment of the internal stellar structure. In the next section, we describe in detail the main assumptions of our parametric spin evolution model.

For simplicity, we assume a dipolar field with strength B_* at the equator of the stellar surface and co-rotating with the star. At larger stellar radii, this dipole enables angular momentum transport with the disk and magnetosphere. We assume values range between 500-3500 G in agreement with previous studies (Johns-Krull 2007) and recent surveys such as Lavail et al. (2017, 2019). The main assumptions for constructing our grid of rotational models are the following:

- **A solid body approach:** We consider a simple approach in our models, assuming that the stars rotate as a solid body with a core and envelope coupled to each other. We neglect any difference in angular momentum between the stellar surface and its stellar interior. Rotation is thus entirely controlled by the external torques. This approach is sufficient for fully convective stars

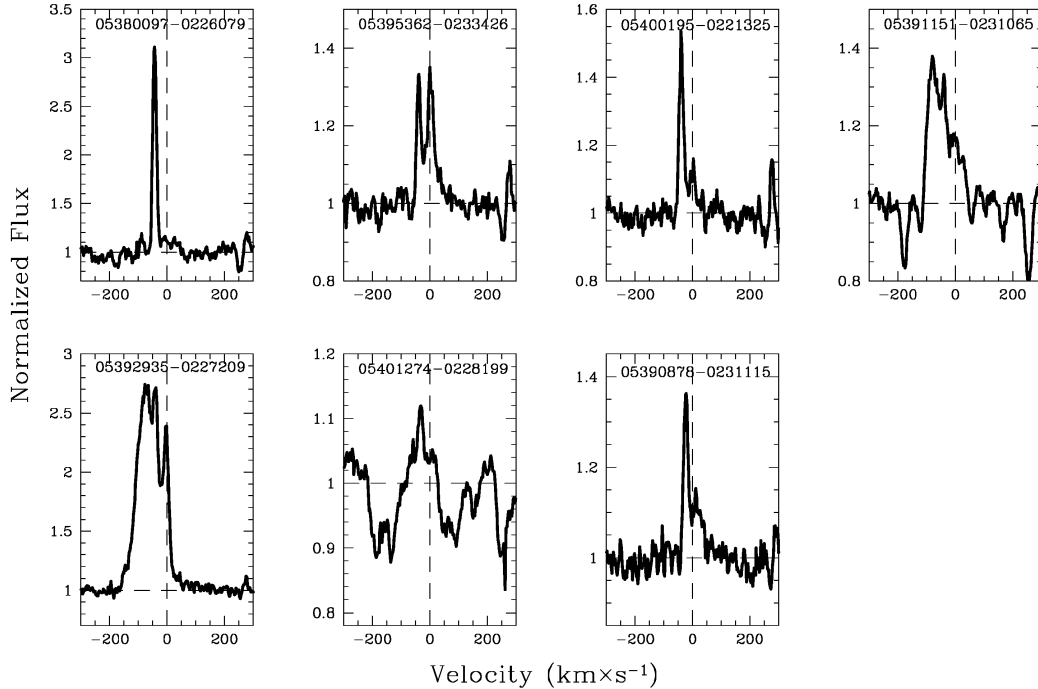


Figure 5. [O I] $\lambda 6300$ residual lines profiles for 7 CTTS found in data archive of Giraffe.

on their Hayashi tracks, although our simplified treatment should be revised for stars with radiative zones in their interiors using a more realistic treatment, similar to the considered redistribution of angular momentum between the two layers (MacGregor & Brenner 1991). We do not expect a strong impact on the rotation rates predicted by our models in the CTTS phase (<10 Myr) because the expected time scale for the core-envelope decoupling interaction starts around ~ 10 -30 Myr (Gallet & Bouvier 2013, 2015).

- **Accretion rate onto the star:** We assume an exponential decay for the accretion rate as a function of age ($\dot{M}_{acc} = \dot{M}_{acc}^{in} e^{-\frac{(t-t_0)}{\tau_a}}$), starting from an initial value \dot{M}_{acc}^{in} at $t_0 = 0.5$ Myr and with a characteristic accretion timescale of $\tau_a = 2.1$ Myr reported by Briceño et al. (2019). Since the exponential relation for the accretor fraction evolution (Briceño et al. 2019) represents a probability that stars in a stellar group have accretion rates above the threshold detection limit, the τ_a obtained from this relation is a statistical proxy for the timescale of the general accretion rate evolution behavior in stellar groups. The accretion process adds angular momentum that is transferred from the disk truncation radius (R_t) toward the stellar surface at a rate of:

$$\tau_{acc} = \dot{M}_{acc} \sqrt{GM_* R_t} \quad (4)$$

R_t denotes the distance at which the magnetic field fully governs the stress in the internal disk. At this location, disk material and the stellar surface share identical rotation. We assumed R_t inside disk corotation, which is computed using the Newton-Raphson method and the equation 15 of Matt & Pudritz (2005a).

- **Stellar winds:** We consider the APSW an important source of angular momentum loss in CTTS (Matt & Pudritz 2008a). Previous studies have shown that open field regions in the magnetic field lead to the formation of ASPW that efficiently removes substantial amounts of angular momentum from the star (e.g., Hartmann & Stauffer 1989, Uzdensky 2004, Pantolmos et al. 2020, Matt et al. 2012, Pinzón et al. 2021). It is assumed that a fraction χ of the mass in the accretion flow is transferred to a stellar wind, i.e., $\dot{M}_{wind} = \chi \dot{M}_{acc}$, providing an efficient angular momentum loss mechanism. The formulation is inspired by the analytic work of Weber & Davis (1967), in which the net torque from a one-dimensional wind is as follows:

$$\tau_{wind} = -\dot{M}_{wind} \Omega_* r_A^2 \quad (5)$$

where \dot{M}_{wind} is the integrated wind mass-loss rate, Ω_* is the angular velocity of the star, and r_A is the Alfvén radius. In our one-dimensional approach, we used the semi-analytical results obtained from

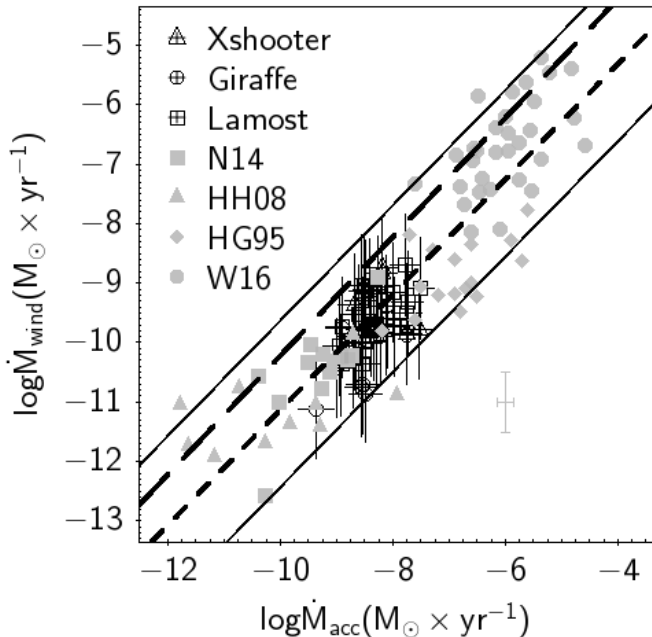


Figure 6. Accretion and mass-loss rates for our sample of CTTS (black crosses) and other studies (gray symbols). Complementary data shown in gray correspond to low mass accretors in Taurus from [Herczeg & Hillenbrand \(2008\)](#), (triangles) active CTTS systems from [Hartigan et al. \(1995\)](#), [Gullbring et al. \(1998\)](#) (diamonds) and selected CTTS from [Natta et al. \(2014\)](#) (squares) and [Watson et al. \(2016\)](#) (circles). The long-dashed line indicates the upper limit given by APSW models of [Matt et al. \(2012\)](#), i.e. $\dot{M}_{wind} = \chi \times \dot{M}_{acc}^\eta$, with $\eta = 1$, and $\chi = 0.6$. The short-dashed line corresponds to the linear regression fit using all the data, which leads to $\eta = (0.97 \pm 0.05)$ and $\chi = 0.04_{-0.02}^{+0.05}$. Upper and lower solid lines represent the 3σ level for the whole sample.

numerical MHD simulations of [Matt & Pudritz \(2008a\)](#):

$$\frac{r_A}{R_*} = K \left(\frac{B_*^2 R_*^2}{\dot{M}_{wind} v_{esc}} \right)^m \quad (6)$$

where $K \approx 2.11$ and $m \approx 0.223$ are dimensionless constants and $v_{esc} = (2GM_*/R_*)^{1/2}$ is the escape velocity from the star.

- **Star-disk interaction:** Along with angular momentum losses through disk winds, CTTS also spin down due to their magnetic interaction with the Keplerian rotating disk (e.g., [Ghosh & Lamb 1978](#), [Koenigl 1991](#), [Collier Cameron & Campbell 1993b](#)). In a scenario of large Reynolds numbers of the star-disk interaction (low diffusion parameter β), the strong coupling between disk matter and stellar magnetic field lines leads to a twisting

of the vertical field component B_z and thus to a spin-down torque given by:

$$\tau_{DL} = \frac{B_*^2 R_*^6}{3\beta R_{co}^3} \left[2 \left(\frac{R_{co}}{R_{out}} \right)^{\frac{3}{2}} - \left(\frac{R_{co}}{R_{out}} \right)^3 - 2 \left(\frac{R_{co}}{R_t} \right)^{\frac{3}{2}} + \left(\frac{R_{co}}{R_t} \right)^3 \right] \quad (7)$$

here $R_{out} = R_{co}(1 + \beta\gamma_c)^{\frac{2}{3}}$ defines the extent of the connected magnetic region. R_{co} is the co-rotation radius, R_t the disk truncation radius, and $\gamma_c = B_\phi/B_z$ characterizes the proportion of magnetic field twisted at the disk's surface at each radial location. We use $\gamma_c = 1$ and $\beta = 10^{-2}$ as fixed parameters in all our simulations ([Matt et al. 2010](#)).

3.2.1. Grid of Rotational Models

The evolution of the stellar rotation rate (Ω_*) is computed by solving the following differential equation:

$$\frac{d\Omega_*}{dt} = \frac{\tau_*}{I_*} - \frac{\Omega_*}{I_*} \frac{dI_*}{dt} \quad (8)$$

where τ_* is the sum of the individual torques due to the accretion, winds, and star-disk interaction as described above, and $I_* = k^2 M_* R_*^2$ is the stellar moment of inertia and k^2 is the gyration radius obtained from the stellar evolutionary models of [Baraffe et al. \(2015\)](#). We note that the accretion rate is incorporated into the calculation of dI_*/dt and used to update M_* .

Using the fourth-order Runge-Kutta method with adaptive step size, we find the solution to the equation (8)³. At each time step of the simulation, we compute the next time step, ensuring changes over the Ω_* solution remain lower than 1% per step.

We use the set of parameters [M_* , B_* , χ , P_{rot}^{in} , \dot{M}_{acc}^{in}] based on the values of Table 3. We use all possible combinations of the parameters, without repetitions, and within the value ranges and steps to build a grid with 2.232×10^6 individual models. For each combination of the five parameters in Table 3, the angular momentum conservation, stellar evolutionary models, and the assumed exponential decay for the accretion rate as a function of age regulate the temporal variation of the synthetic rotational values (e.g., angular velocity, $v \sin(i)$) estimated in our grid. Simulations start at 0.5 Myr and end at 15 Myr, the age at which there are some long-lived CTTS. Nevertheless, statistically, the typical age when the gas component of the disk has

³ The models are available on GitHub in the following link: [Rotational-models-of-CTTS](#)

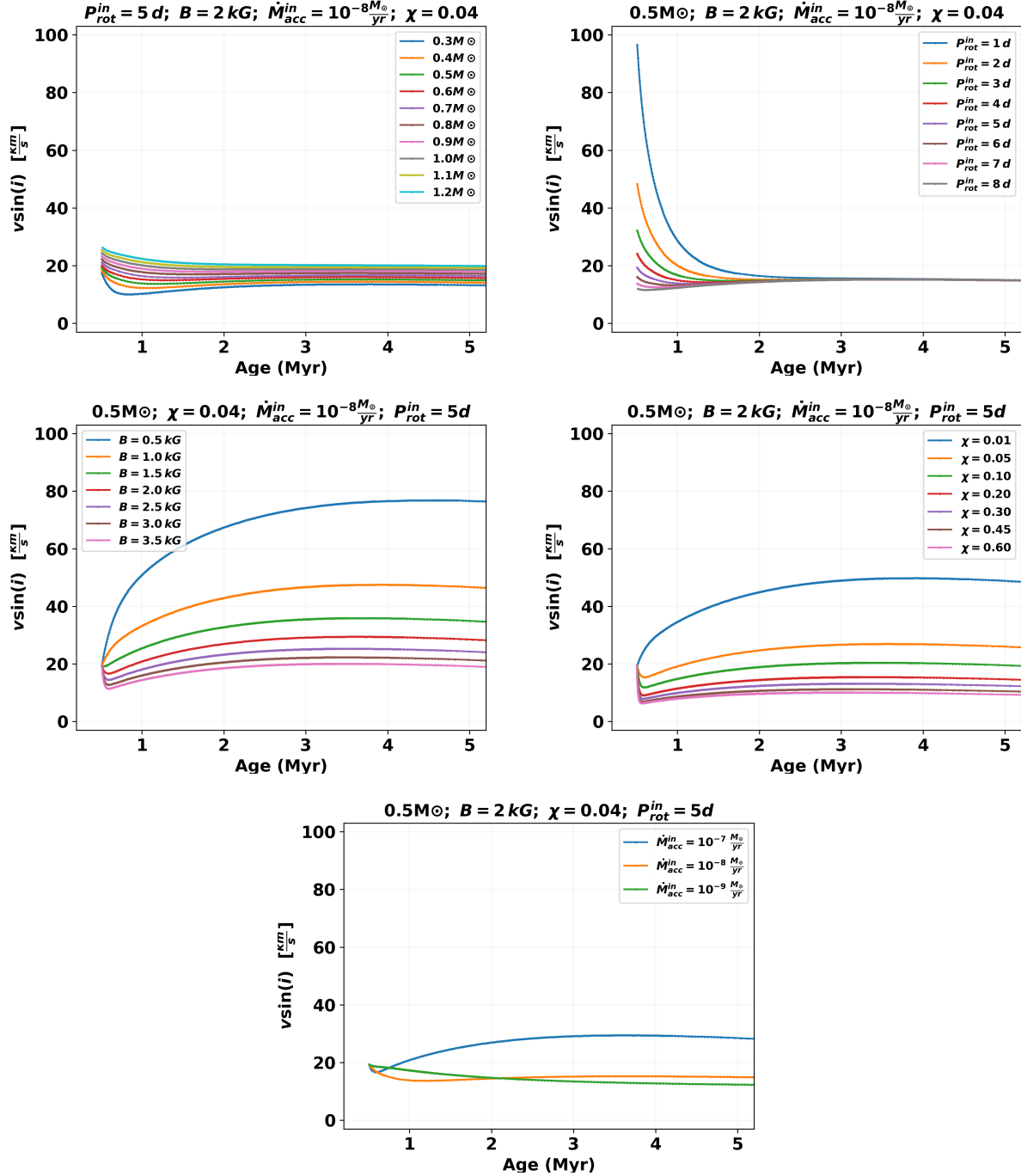


Figure 7. Spin evolutionary tracks represented as $v \sin(i) = \frac{\pi}{4} v_{\text{rot}}$ as a function of age for individual cases. The title of each panel shows the fixed parameters. Meanwhile, the legend colors represent different cases for a respective variable in the models.

been dissipated is around 5 Myr (Carpenter et al. 2006, Hernández et al. 2008). Given a simulation, both the angular velocity (stellar period) and the mass accretion rate evolve with time.

3.3. $v \sin(i)$ synthetic distributions

The rotation rates given by our grid of models are related to the projected rotational velocities through the previous knowledge of spin-axis orientation. By assuming that the spin-axes of objects are randomly oriented, and utilizing the inclination average method proposed by Chandrasekhar & Münch (1950), the projected rotational velocity can be expressed as $v \sin(i) = \frac{\pi}{4} R_* \Omega_*$, where R_* is the stellar radius and Ω_* is the angular

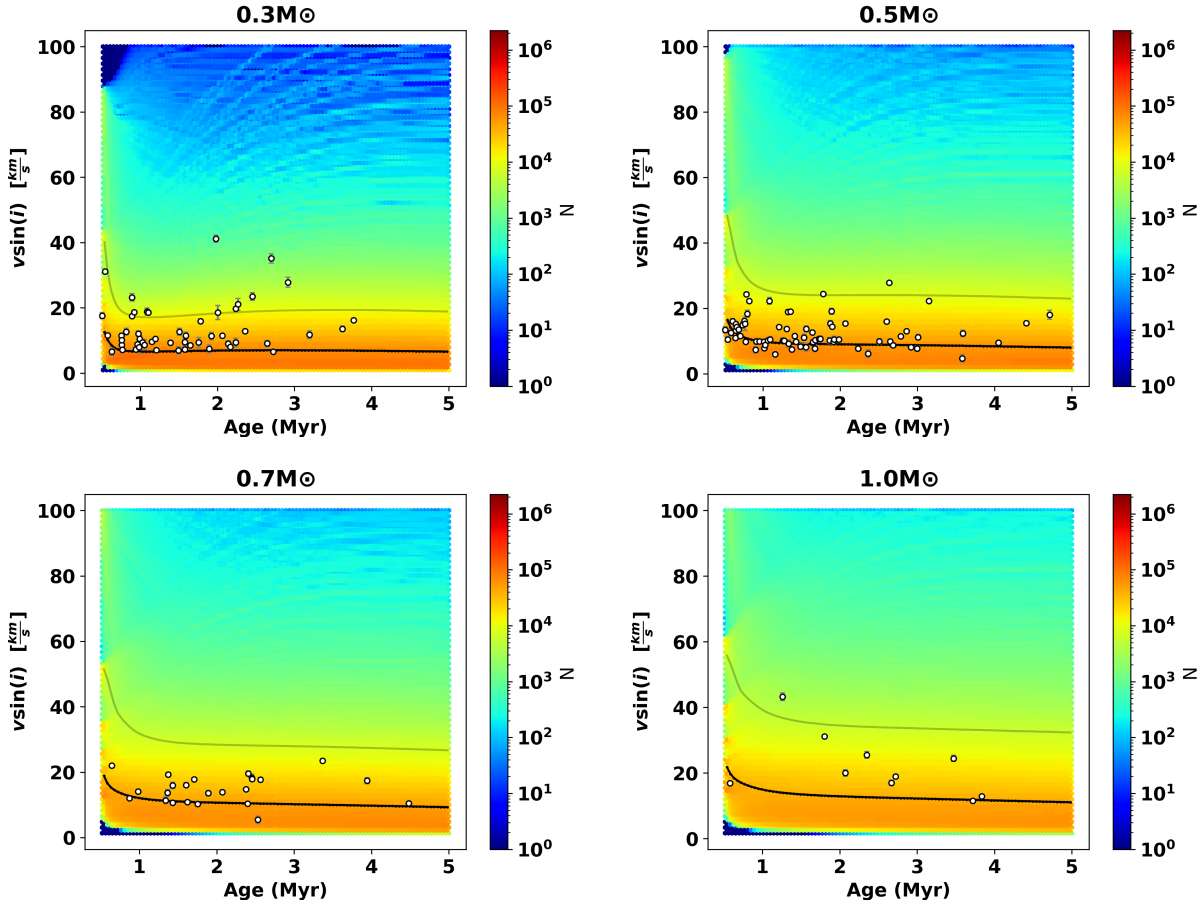


Figure 8. Grid of models illustrated as a density plot of $v \sin(i) = \frac{\pi}{4} v_{rot}$ as a function of the age, in different values of mass. The black line shows the grid’s median $v \sin(i)$, while the gray line contains 90% of the models below it. The color scale represents the number of models per hex bin pixel. The white dots represent the $v \sin(i)$ and age for the CTTS sample.

velocity of the star.

In Figure 7, we show individual evolutionary tracks of $v \sin(i)$ for specific cases of the parameter set. While in Figure 8, we display the complete grid of models for masses of 0.3, 0.5, 0.8, and $1.0 M_{\odot}$. In each panel, the color scale represents the number of models enclosed in each hexagonal bin pixel of the $v \sin(i)$ versus age diagram. We have included the 90th percentile and the median per pixel indicated with grey and black lines, respectively.

The panels in Figure 8 show a decreasing trend of the median of $v \sin(i)$ with age. Despite the wide range of initial conditions considered in Table 3, most solutions lie on the slow rotator regime with rotation below 10% of the break-up limit as expected for CTTS. Synthetic velocities increase with stellar mass, as confirmed by the gradual growth of the 90th percentile of the $v \sin(i)$ distributions, plotted with a gray line at each panel of Figure 8. We also note that rotational equilibrium

Table 3. Input parameters of the models, their ranges, and steps.

Parameters	Min	Max	Step
P_{rot}^{in} (days)	1	8	1
\dot{M}_{acc}^{in} ($M_{\odot} \text{ yr}^{-1}$)	10^{-10}	10^{-7}	$10^{-0.2}$
M_* (M_{\odot})	0.3	1.2	0.1
B_* (G)	500	3500	100
χ	0.01	0.60	0.01

is reached very rapidly, particularly for low-mass stars (< 1 Myr). For comparison purposes, we have added the rotation rates measured for our sample of CTTS. With a few exceptions, especially for $0.3 M_{\odot}$, the bulk of $v \sin(i)$ values remains below the 90th percentile of our simulations, reaching a rotational locked state by the end of the Hayashi track (< 3 Myr) in agreement with previous studies (Gallet & Bouvier 2013).

3.4. Spin-torque equilibrium

The total torque on the system is the sum of the accretion, winds, and star-disk interaction torques:

$$\tau_* = \tau_{acc} + \tau_{wind} + \tau_{DL} \quad (9)$$

Values of $\tau_* = 0$ are also known as the torque equilibrium state. In the APSW scenario, stellar rotation evolves rapidly (<1 Myr) toward an equilibrium state in which angular momentum transferred toward the star by the disk accretion is balanced with that transferred outward via winds and magnetic star-disk interaction (Matt & Pudritz 2005b, Matt et al. 2012). For bonafide samples of CTTS with reliable masses, ages, accretion, and rotation rates, the determination of this equilibrium state permits indirectly inferring the response of the wind to different magnetic strengths and topologies and allows for searching statistical trends between the branching ratio and the stellar magnetic field.

Panel A of Figure 9 reveals that the torque equilibrium state, on average, is reached at 1.5 Myr. On the other side, panels B and C of Figure 9 also indicate that an equilibrium state can be achieved with higher values of B_* and χ at ages earlier than 1.5 Myr. The majority of the models are placed on the equilibrium zone, especially stars older than 1.5 Myrs, to ensure that equilibrium is rapidly reached, a fact consistent with previous studies (Yi 1994, Armitage & Clarke 1996, Matt et al. 2012).

Interestingly, stellar winds can achieve equilibrium spin rates during the Hayashi track when magnetic field strengths and branching ratios are large. In §4, we discuss this result based on statistical techniques in depth.

3.5. Observations and models comparison

With the aim of conducting careful comparisons between observations and models, we implement Bayesian techniques. We use our sample of CTTS (§2.1), together with the models described in §3.2, to explore the interplay between stellar magnetic field strength and the branching ratio χ in young accreting systems during the first Myr of their stellar evolution. To perform the comparison, we use the observed rotation rates compiled in Table 1 and the rotation rates provided by the models, varying the parameters in the ranges shown in Table 3. Below we describe the use of the Bayesian technique in more detail.

3.5.1. Stellar magnetic field and wind mass-loss rate evolution: forward modeling

We carry out a statistical study to understand the changes in the physical parameters related to the evolution of the rotation velocities of young stars. In order to perform an analysis as robust as possible, we split our sample of CTTS described in §2.1 into four age bins as follows: bin 1: 0-1 Myr (62 stars), bin 2: 1-2 Myr (68 stars), bin 3: 2-3 Myr (40 stars), and bin 4: 3-13 Myr (30 stars). We use the compiled $v \sin(i)$ measurements (see §2.2) to build the corresponding distribution of rotational velocities for each age bin. These distributions are shown in Figure 10.

First, we selected from the grid model generated in section 3.2 an ensemble of models for each age bin. Thus, we have four ensembles of models, one per each CTTS sample. Then, we reproduce the observed $v \sin(i)$ histograms for each age bin using the Approximate Bayesian Computation (ABC) method, a statistical approach that compares models with observed data (e.g., Marjoram et al. 2015, Manzo-Martínez et al. 2020). This is achieved by randomly selecting $v \sin(i)$ values from the respective ensemble of models previously selected. For each $v \sin(i)$ distribution of Figure 10, we keep and stack the values that fall within the range of the observations and discard those that fall out of this range. We continue selecting theoretical $v \sin(i)$ values randomly until we complete one realization, meaning that the observed histogram is exactly reproduced (e.g. Turner & Van Zandt 2012). Due to the limitations of the ABC method, for each realization, only one parameter (B_* or χ) can be chosen to obtain the posterior distribution. If B_* is chosen, a fixed value of $\chi = 0.3$ is used (Case A), representing the minimum value for spin equilibrium (Ireland et al. 2020). If χ is chosen, B_* is fixed at 2000 G (Case B), the average magnetic field strength from CTTS measurements (Johns-Krull 2007). This analysis is repeated 100 times for each age bin to build statistically robust distributions of the chosen parameter.

In the ABC analysis, we use $M_* = 0.5M_\odot$ since it is the median stellar mass from the sample of stars used in each bin. We decided to use a representative value of stellar mass for this analysis since the mass range of the CTTS sample is relatively narrow (e.g., an interquartile range of $\sim 0.2 M_\odot$), and we do not have enough CTTS to additionally split them into several mass bins. We also have included the observed distribution of mass accretion rates discussed in §3.1.2 as a constraint. For this purpose, we separate the sample of stars with accretion measurements into the same age bins defined in this section and use the corresponding \dot{M}_{acc} distribution at each age bin as a prior distribution. Figure 11 shows the distributions of mass accretion rates for

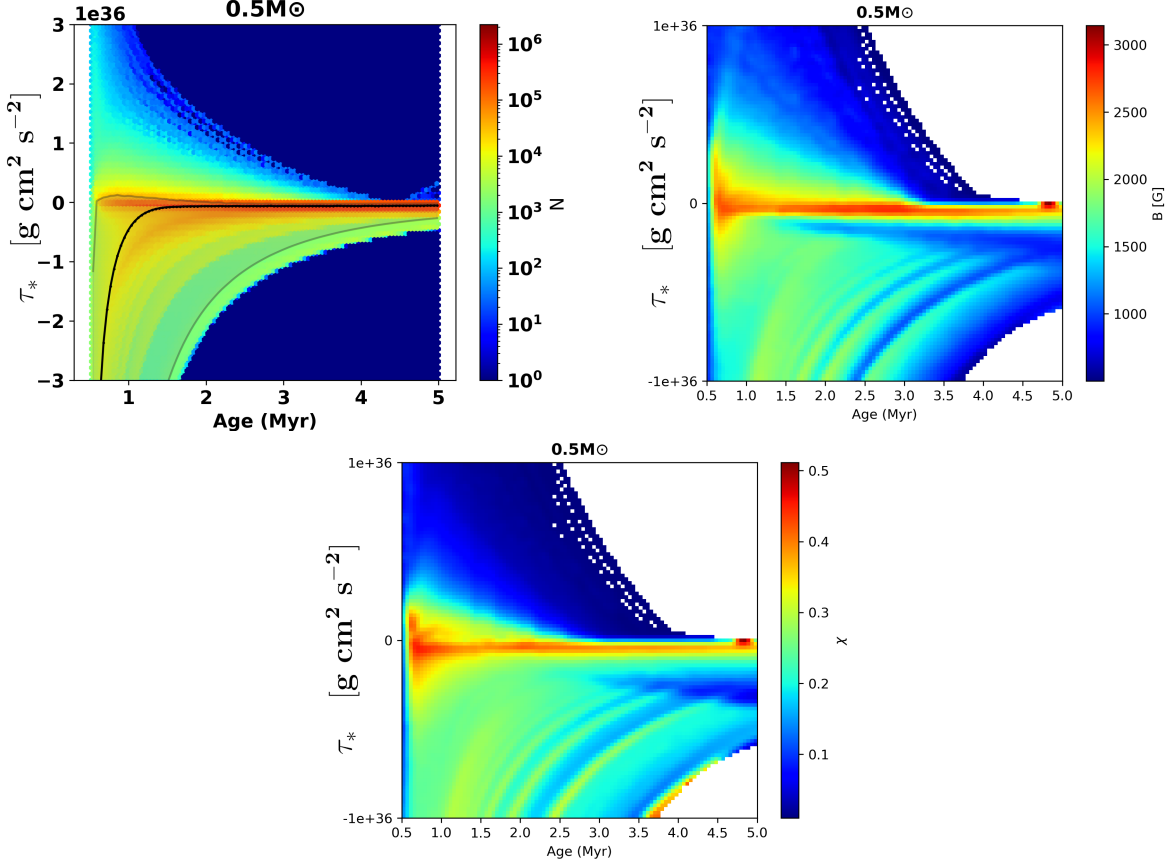


Figure 9. Rotational grid for the case $0.5 M_{\odot}$ obtained using the set of input parameters in Table 3. (1) The distribution of the total torque applied onto the stars as a function of age. The color bar represents the number of models per bin. The median of the models is represented as the black line. The grey zone contains 90% of the models. (2) Distribution of magnetic stellar field strengths versus age. The color bar illustrates the median value per bin. (3) Distribution of branching ratio versus age. Similarly to (2), the color bar represents the median values per bin.

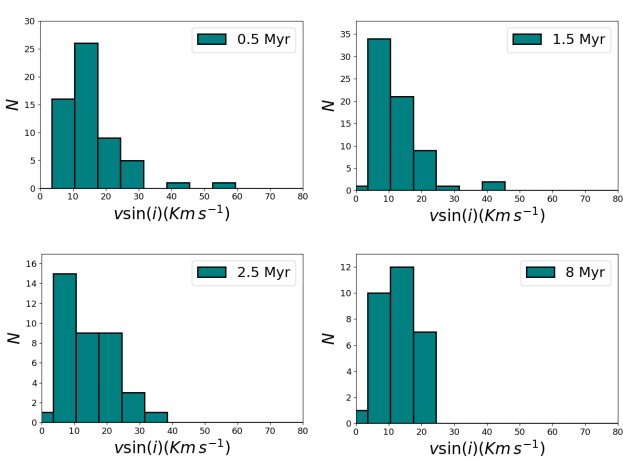


Figure 10. Rotational velocity distributions for the age bins described in §3.5.1.

each bin. It can be seen that, as the age increases, the distributions move towards lower values of accretion,

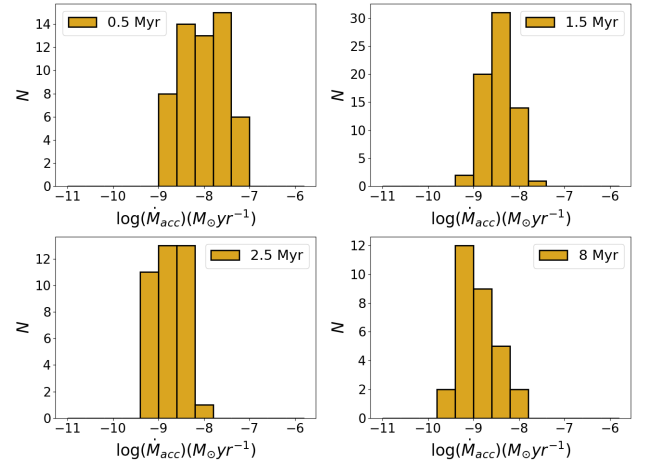


Figure 11. Mass accretion rate distributions for the age bins defined in the Bayesian analysis.

as expected (e.g. Hartmann et al. 2016, see §3.1.2 for more discussion). The randomly selected \dot{M}_{acc} values

used in the ABC analysis follow the corresponding cumulative distribution of accretion rates for each age bin. Finally, we obtained the posterior distribution of χ and B_* (see Figure 12). Using the 100 realizations of the ABC techniques, we construct the histograms using the mean and the standard deviation for each bin of χ and B_* , respectively.

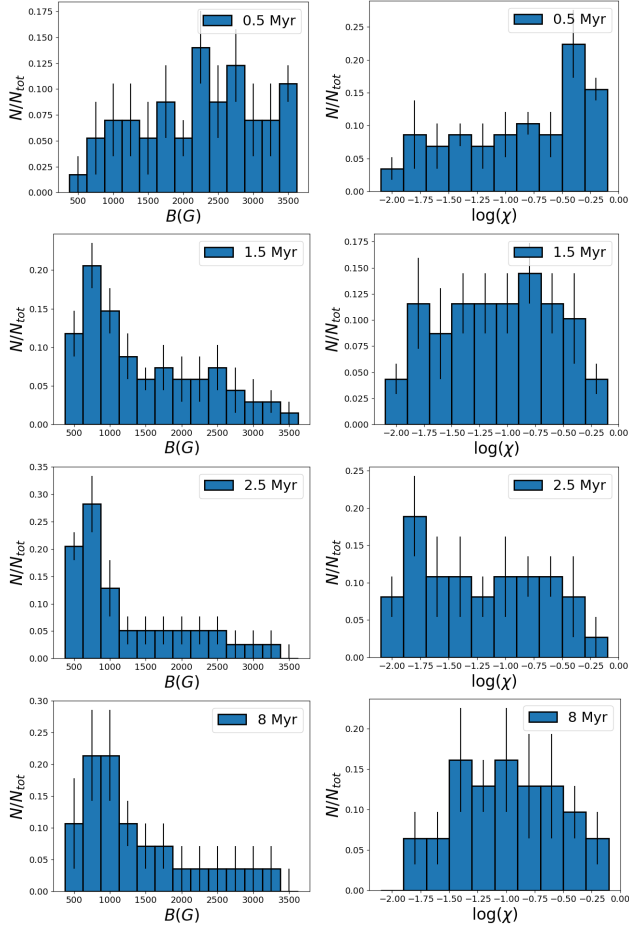


Figure 12. Evolution of B_* and χ in young stars revealed by the ABC analysis. The left panel shows the posterior distributions of magnetic field strength B_* for different age bins, obtained assuming a fixed $\chi = 0.3$ (Case A). The right panel shows the posterior distributions of $\log(\chi)$ for different age bins, obtained by fixing $B_* = 2000$ G. The results suggest that one of the two parameters, either B_* or χ , likely decreases with age, while other remain fixed play a significant role in the rotational evolution of young stars.

Figure 12 shows the resulting distribution for (1) B_* (left column: Case A) and (2) $\log(\chi)$ (right column: Case B) obtained from our Bayesian analysis. In these plots, the age increases downwards.

Based on this comparison, we obtain that B_* distributions with systematically smaller values can reproduce

better the observed $v \sin(i)$ distributions when we move to older bin ages. Specifically, for the stellar magnetic field, the distribution at bin 1 shows that median value is ~ 2100 G, and the median in bins 2, 3, and 4 moves toward lower values. This suggests that B_* decreases as the stars evolve during the pre-main sequence. Similarly, for the branching ratio, the distribution in bin 1 shows a median value at $\chi = 0.15$, and the median values of the 2 and 3 distributions move to lower branching ratios than the first bin. At bin 4, the peak appears slightly shifted toward larger χ values ($\chi \sim 0.04$) with respect to bin 3. These results are shown more clearly in Figure 13, in which we plot the cumulative distributions of the data from Figure 12.

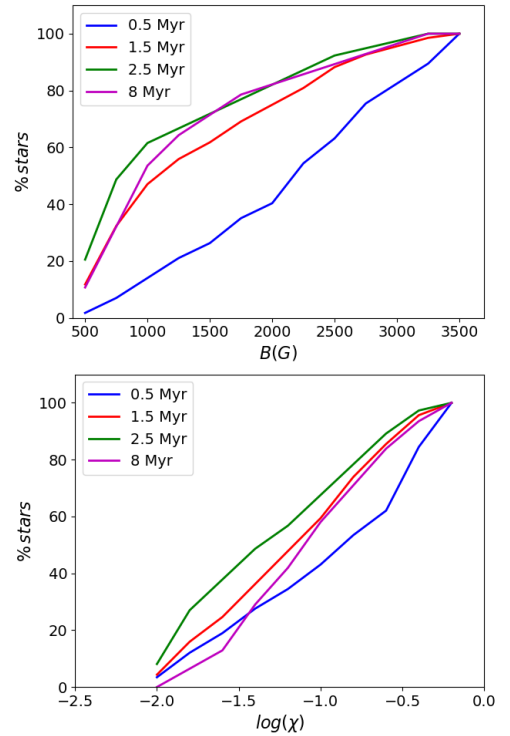


Figure 13. Cumulative distributions for B_* (upper panel) and $\log(\chi)$ (lower panel), for bin 1 (blue), bin 2 (red), bin 3 (green), and bin 4 (magenta).

The histograms in Figure 12 suggest a gradual decrease in the branching ratio and magnetic field strength for the first three age bins. The slight increase in the branching ratio (χ) from bin 3 to bin 4 is unexpected. It must be noticed that the oldest bin has an age spread of 3-13 Myr and is the smallest sample of the different bins. If the sample in bin 4 is not a representative distribution for $v \sin(i)$ in this age interval, the results for χ from the ABC method could be biased towards

values that describe this incomplete sample.

In order to test the robustness of our results with the ABC technique, particularly the impact of low numbers in the sample used in bin 4, we performed an additional Bayesian test using synthetic prior distributions for $v \sin(i)$. We generated random Gaussian distributions for each age bin, using the corresponding median value and the median absolute deviation (MAD) of the observed $v \sin(i)$ histograms shown in Figure 10. We demonstrate in Appendix B that the general trends seen in Figure 12 hold, and they are independent of the number of stars in each bin. Further details of this test can be found in Appendix B. Although our results suggest that the observed increase of B_* and χ toward bin 4 (Figure 12) is not a statistical fluctuation caused by low numbers, this result should be taken carefully since: (1) The sample of CTTS in the last bin could not be as representative as in the younger bins. In particular, given the variable nature of TTS, slow accretors or CTTS approaching the end of their accretion phase (Briceño et al. 2019, Thanathibodee et al. 2022) could not be included in the last bins; (2) A wide age range (3-13 Myr) is considered in the last bin, in which the stars significantly change their properties during the pre-main sequence evolution. However, torque equilibrium in the system is reached earlier than 3 Myr, and models beyond this age do not change significantly (see figure 8); (3) We assume that the parameters γ_c and β are constant. These parameters are related to the magnetic connection between the star and the disk, which might change, together with the complexity of the magnetic field, during the evolution of the star; (4) The models ignore the changes in the inner stellar structure, particularly, the core-envelope decoupling is not considered in the models, which might impact the angular momentum evolution at bin 4. Some of these effects are not so important for very young low-mass stars, however, solar-type stars are expected to develop a radiative core at the end of the Hayashi track (Iben 1965). Exploring these effects' impact is out of this paper's scope.

We applied a Kolmogorov-Smirnov (K-S) test, which is used to determine if two samples are drawn from the same distribution, to the B_* and $\log(\chi)$ posterior distributions obtained from the ABC analysis. The p values are shown in Table 4. For bins 1 and 2, we find the low p values of 0.05% and 5%, for B_* and $\log(\chi)$, respectively, suggest evolution of both parameters, as discussed above. In contrast, for B_* , the high p value between bin 3 and bin 4 shows that there is barely an

Table 4. K-S test and p values .

Bin pairs	parameter	K-S	p-value
1-2	B_*	0.35	0.0005
	$\log(\chi)$	0.23	0.05
2-3	B_*	0.16	0.45
	$\log(\chi)$	0.13	0.73
3-4	B_*	0.16	0.68
	$\log(\chi)$	0.24	0.20

evolution, which suggests that most of the stars have reached a state in which the strength of their magnetic field has decreased to lower values. For $\log(\chi)$, the difference between bins 3 and 4 seems more clear; the possible explanations for these differences are also discussed above.

Our results suggest that the median of B_* and $\log(\chi)$ might be decreasing as the age of the bins increases, this implies that both parameters could evolve during the first million years. These results remain consistent under testing with back-forward models. For additional information, please refer to the model insights in Appendix C. Additional measurements of magnetic fields and stellar winds are needed to confirm the observed trends.

4. DISCUSSION

4.1. Binarity

We make a quality astrometric selection of the CTTS using the Re-normalized unit weighted error (RUWE) reported by *Gaia* DR3. For the selection, we use RUWE values less than 1.4, suggested by Lindgren et al. (2020). However, Stassun & Torres (2021) and Kounkel et al. (2021) confirmed that RUWE values from 1.0 to 1.4 may contain unresolved binary systems.

One of the main consequences of having binary stars in our sample will be the inconsistency of the physical parameters (e.g., Rotation rates, masses, ages, etc.). In that sense, we have cleared our sample of possible close companions systems using the spectroscopic binaries reported by (Kounkel et al. 2019) and visual binaries reported by Tokovinin et al. (2020). Also, we did not find discrepancies in rotation rates for CTTS groups by mass and age that could indicate the presence of binaries. As a double-check test, we inspected each LC available in TESS (§3.1.1), and as a result, we did not detect signatures of eclipsing binaries in the sample.

The RUWE and the LCs inspection can not reject all multiple systems in our sample, particularly unresolved

systems. However, we expect that binary systems do not dominate our sample and, thus, do not affect our results.

4.2. Clues about the branching ratio

Several studies have explored the branching ratio parameter from a numerical perspective to explain the slow rotations in CTTS. At the same time, only some efforts have focused on the observational viewpoint. For example, Hartmann & Stauffer (1989), Matt & Pudritz (2005), Matt et al. (2012) have suggested that if there is a stellar wind with a sustained mass-loss rate of about 0.1 of the accretion rate, the wind can carry away enough angular momentum to achieve a stellar-spin equilibrium. Matt & Pudritz (2008a) suggested a hard upper limit of $\chi \leq 0.6$. Cranmer (2008), by his part, predicts a maximum of 0.014. Gallet et al. (2019) studied two cases where they argued that a branching ratio $\chi = 0.01$ would favor the stellar wind theory. However, simulations would require stronger dipolar magnetic fields to reproduce the rotation rates, while $\chi = 0.1$ requires weaker dipolar fields that are commonly observed. Ireland et al. (2020) suggest that $\chi > 0.3$ is required to achieve spin-equilibrium in their simulated cases. Particularly, for the BP Tau star, they predict a $\chi \approx 0.25$ to achieve an equilibrium between the wind and accretion torques. Pantolmos et al. (2020) predict that winds should eject more than 0.1 of the mass-accretion rate to counteract the stellar spin-up due to accretion. Gehrig et al. (2022) reproduce the observed rotational period of most young stars with values less than 0.05. Independently of their numerical approaches and strategies to describe the star-disk interactions and winds, nowadays, no consensus has been reached. Observational analyses of Hartigan et al. (1995) have found that χ can reach up to 0.2, but most values are below 0.02 in all ages between 1 and 10 Myr. Measurements provided by this work could help to contribute to a general perspective of the expected χ in CTTS.

We have 37 stars with available χ measurements that simultaneously hold an estimation of age (Table 1). These stars were utilized in Figure 14 to investigate the relationship between χ and age (left panel). As seen in the histogram (right panel), branching ratio values tend to be below 0.1, and the most likely values are around 0.04 – 0.05. Even though few data are displayed in Figure 14, within the uncertainties, our data suggest that strong stellar wind with a mass loss rate greater than 0.1 of the accretion rate is possible at earlier ages (< 3 Myr).

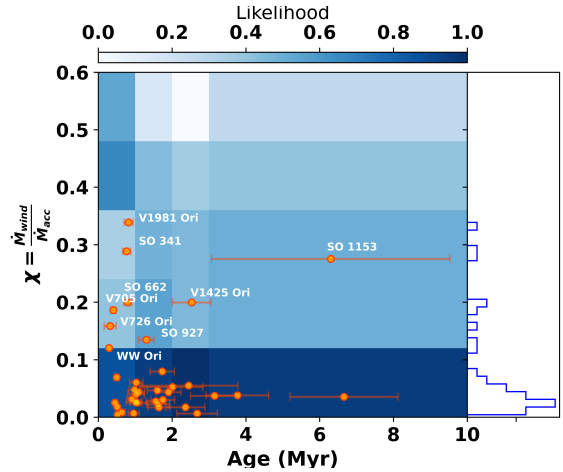


Figure 14. Branching ratio for measured Classical T Tauri stars versus age (left panel). The background map illustrates the density of the posterior distribution of χ given by the ABC analysis. We display their name for those stars with $\chi > 0.1$. The distribution of the branching ratio represented with the histogram on the right side exhibits a pronounced peak at $\chi = 0.04$ as expected from data in Figure 6.

The ABC analysis in §3.5.1 plus measurements reported here could suggest a possible trend for the branching ratio with age. In the future, supplementary surveys of accretion and mass-loss rates in CTTS (e.g., Kounkel et al. 2023) will improve the sampling and allow us to understand better the nature and strength of the APSW mechanism at the early stages of the stars.

5. SUMMARY AND CONCLUSIONS

In this work, we developed one-dimensional numerical models of the spin evolution of CTTS, which allowed us to build a comprehensive grid of specific cases for CTTS. We build approximately two million simulations, varying physical parameters such as magnetic field, wind, accretion, initial rotation periods, and mass. Our models allow for the first time to study how the magnetic field strength (B_*) and branching ratio (χ) change in relation to rotation rates and ages. The results are broadly consistent with the APSW picture and predict a steady evolution of B_* and χ during the CTTS phase. Below we list the results of this work:

- Ninety percent of our model’s grid is compliant with $v \sin(i)$ rotation rates below 50 km s^{-1} .
- Using the observed rotation and accretion rates as prior distributions, we performed a Bayesian analysis that suggests a decreasing trend of χ and B_* intensities with age.

- The models indicate that strong dipolar magnetic field components and higher branching ratios would achieve an effective equilibrium state of torque at the first stages of the evolution in CTTS (< 1.5 Myr). However, at least for the branching ratio, from the observational measurements and the posterior distributions of the ABC analysis, we speculate that $\chi < 0.1$ would be more likely than $\chi > 0.1$.
- Models suggest a branching ratio decreasing with age, in particular, during the first 2 Myr when a pronounced peak for $\chi=0.04$ is observed. This result is in agreement with our measurements using a diverse sample of CTTS (Figure 6) suggesting that small χ values up to 10% of the APSW upper limit are capable of extracting enough angular momentum from the CTTS system.

ACKNOWLEDGMENTS

A special thanks to Lee Hartmann, Jerome Bouvier, Luis Aguilar, and the anonymous referee for their helpful opinions and recommendations for improving the article. J.S. acknowledges from the CONACYT by fellowship support in the Posgrado en Astrofísica graduate program at Instituto de Astronomía UNAM. J.H. acknowledges support from the National Research Council of México (CONACyT) project No. 86372 and the PAPIIT UNAM projects IA102921, IA102319, and CG-101723. E.M.M. acknowledges the support from a CONACyT postdoctoral grant. K.M. is funded by the European Union (ERC, WANDA, 101039452). Views and opinions expressed are however those of the author(s) only and do not necessarily reflect those of the European Union or the European Research Council Executive Agency. Neither the European Union nor the granting authority can be held responsible for them. C.R.-Z. acknowledges support from project CONACyT CB2018 A1-S9754 and the PAPIIT UNAM project IN112620. A.B. acknowledges partial funding by the Deutsche Forschungsgemeinschaft Excellence Strategy - EXC 2094 - 390783311 and the ANID BASAL project FB210003.

This paper includes data collected with the TESS mission, obtained from the MAST data archive at the Space Telescope Science Institute (STScI). Funding for the TESS mission is provided by the NASA Explorer

Program. Funding for the Sloan Digital Sky Survey IV has been provided by the Alfred P. Sloan Foundation, the U.S. Department of Energy Office of Science, and the Participating Institutions. SDSS-IV acknowledges support and resources from the Center for High-Performance Computing at the University of Utah. The SDSS website is www.sdss.org. SDSS-IV is managed by the Astrophysical Research Consortium for the Participating Institutions of the SDSS Collaboration including the Brazilian Participation Group, the Carnegie Institution for Science, Carnegie Mellon University, Center for Astrophysics — Harvard & Smithsonian, the Chilean Participation Group, the French Participation Group, Instituto de Astrofísica de Canarias, The Johns Hopkins University, Kavli Institute for the Physics and Mathematics of the Universe (IPMU) / University of Tokyo, the Korean Participation Group, Lawrence Berkeley National Laboratory, Leibniz Institut für Astrophysik Potsdam (AIP), Max-Planck-Institut für Astronomie (MPIA Heidelberg), Max-Planck-Institut für Astrophysik (MPA Garching), Max-Planck-Institut für Extraterrestrische Physik (MPE), National Astronomical Observatories of China, New Mexico State University, New York University, University of Notre Dame, Observatório Nacional / MCTI, The Ohio State University, Pennsylvania State University, Shanghai Astronomical Observatory, United Kingdom Participation Group, Universidad Nacional Autónoma de México, University of Arizona, University of Colorado Boulder, University of Oxford, University of Portsmouth, University of Utah, University of Virginia, University of Washington, University of Wisconsin, Vanderbilt University, and Yale University. Guoshoujing Telescope (the Large Sky Area Multi-Object Fiber Spectroscopic Telescope LAMOST) is a Major National Scientific Project built by the Chinese Academy of Sciences. Funding for the project has been provided by the National Development and Reform Commission. LAMOST is operated and managed by the National Astronomical Observatories, Chinese Academy of Sciences.

Facilities: TESS, APOGEE-2, *Gaia*-DR3, X-Shooter, GIRAFFE, and LAMOST.

Software: Numpy (Harris et al. 2020), Matplotlib (Hunter 2007), Astropy (Astropy Collaboration et al. 2013), Molecfit (Kausch et al. 2015).

APPENDIX

A. LAMOST DATA ARCHIVE SUMMARY

In this Appendix, we compiled the low-resolution plots and table of sources with [O I] $\lambda 6300$ line available in our study of CTTS.

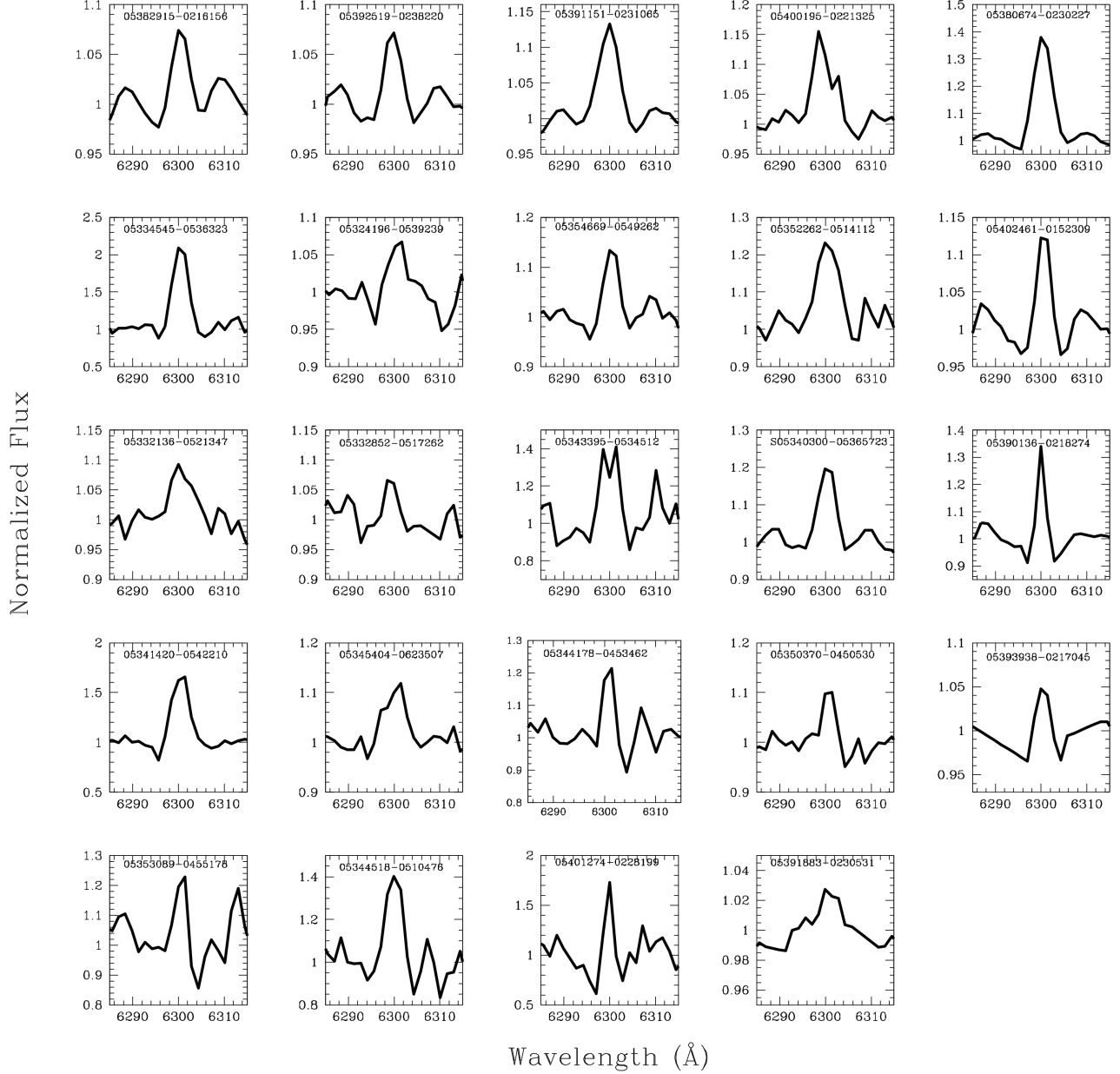


Figure 15. [O I] $\lambda 6300$ Residual lines profiles for 24 CTTS found in data archive of LAMOST.

Table 5. LAMOST Summary of archival data.

2MASS ID	Spectral Resolution	Obs. Date (UT)	Exp. time (s)	SNR ^a	Plan ID
05334545-0536323	1800	2013-11-20T17:26:00	1800.0	4.09	VB081S05V1
05324196-0539239	1800	2013-11-20T17:26:00	1800.0	24.66	VB081S05V1
05354669-0549262	1800	2013-11-20T17:26:00	1800.0	16.0	VB081S05V1
05352262-0514112	1800	2013-11-20T17:10:00	1800.0	13.83	VB081S05V1
05332136-0521347	1800	2013-11-20T17:10:00	1800.0	20.7	VB081S05V1
05332852-0517262	1800	2013-11-20T17:10:00	1800.0	16.21	VB081S05V1
05343395-0534512	1800	2013-11-20T18:24:00	1800.0	3.59	VB081S05V2
05340300-0536572	1800	2013-11-20T18:24:00	1800.0	38.85	VB081S05V2
05341420-0542210	1800	2013-11-20T18:24:00	1800.0	7.1	VB081S05V2
05345404-0623507	1800	2013-11-20T18:24:00	1800.0	19.61	VB081S05V2
05344178-0453462	1800	2013-11-20T18:08:00	1800.0	13.3	VB081S05V2
05350370-0450530	1800	2013-11-20T18:08:00	1800.0	31.88	VB081S05V2
05353089-0455178	1800	2013-11-20T18:08:00	1800.0	11.25	VB081S05V2
05344518-0510476	1800	2013-11-20T18:08:00	1800.0	4.96	VB081S05V2
05401274-0228199	1800	2015-03-01T12:13:00	1800.0	2.78	HD053813S011009V01
05391883-0230531	1800	2016-12-15T17:01:00	1800.0	13.19	HD054602S041606V01
05402461-0152309	1800	2017-01-01T14:26:00	4500.0	101.73	GAC085S03B1
05390136-0218274	1800	2017-01-01T14:26:00	4500.0	121.31	GAC085S03B1
05393938-0217045	1800	2017-01-01T14:26:00	4500.0	180.07	GAC085S03B1
05382915-0216156	1800	2017-01-01T14:26:00	4500.0	224.63	GAC085S03B1
05380674-0230227	1800	2017-01-01T14:26:00	4500.0	119.59	GAC085S03B1
05400195-0221325	1800	2017-01-01T14:26:00	4500.0	49.09	GAC085S03B1
05391151-0231065	1800	2017-01-01T14:26:00	4500.0	136.68	GAC085S03B1
05392519-0238220	1800	2017-01-01T14:26:00	4500.0	233.1	GAC085S03B1

^aThe reported SNR was estimated at the r' Sloan band in which the effective central wavelength corresponds to 620.4 nm.

B. ABC ANALYSIS ADDITIONAL TEST

We performed an additional test using the ABC technique to explore the robustness of the results discussed in §3.5.1. In particular, to explore if the increase of $\log(\chi)$ from bin 3 to bin 4 is an effect of low numbers in the last bin. For this purpose, for each $v \sin(i)$ distribution shown in Figure 10, we used the corresponding median value and the median absolute deviation to build synthetic random Gaussian distributions using 200 points. The median and MAD values are (13.6, 3.41), (10.48, 2.17), (13.01, 4.98), and (12.89, 5.13) km s^{-1} , for bin 1, bin 2, bin 3, and bin 4, respectively. The artificial Gaussian distributions are shown in Figure 16.

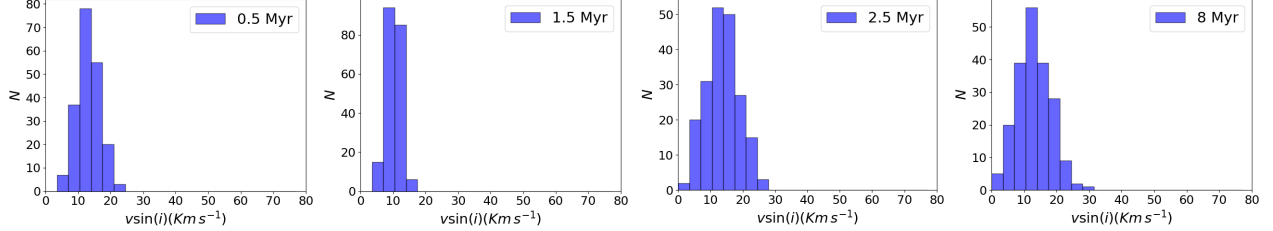


Figure 16. Synthetic distribution of $v \sin(i)$ at each age bin.

In this ABC test, we performed 100 realizations to fill the synthetic $v \sin(i)$ histograms shown in Figure 16. The obtained posterior distributions are shown in Figure 17. For $\log(\chi)$, we also find a gradual transition from high to low branching ratios from bin 1 to bin 3, similar to what is seen in Figure 12. In addition, the increase in values of $\log(\chi)$ from bin 3 to bin 4 also is present. For the magnetic field strength B_* , the posterior distributions are the same as the corresponding distributions from Figure 12. Since we use more complete $v \sin(i)$ samples to be forward modeled, the standard deviation, represented with vertical bars in each bin value of $\log(\chi)$ and B_* , is smaller compared with the results seen in Figure 12. This test confirms that the observed increase, in particular for $\log(\chi)$ from bin 3 to bin 4, is not a consequence of low numbers in the $v \sin(i)$ sample used in bin 4. The interpretation of this result, as well as possible explanations, are discussed in §3.5.1.

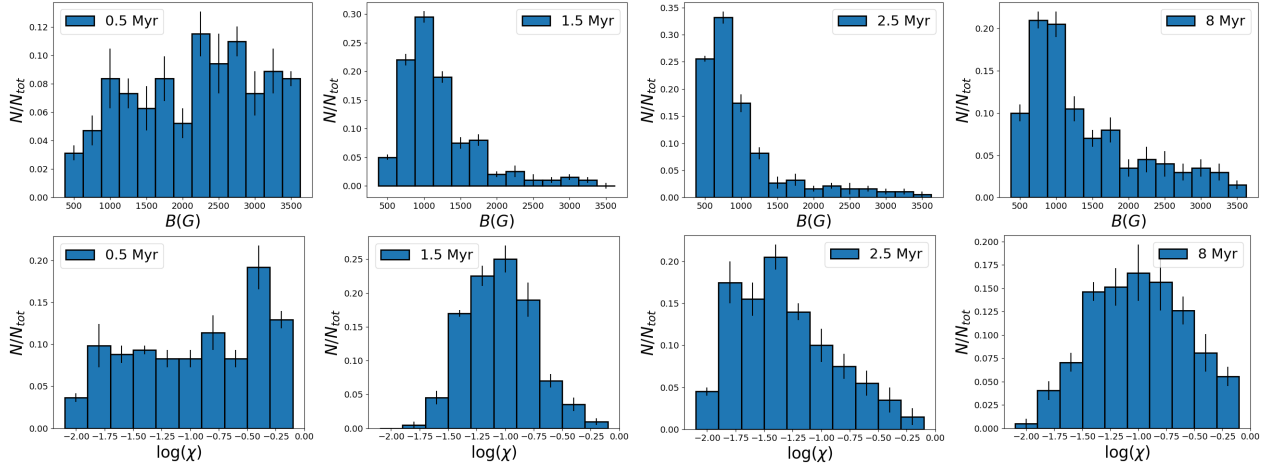


Figure 17. Distributions of parameters at each age bin for the test.

C. AUTO-CONSISTENCY OF ABC RESULTS (ABC BACK-FORWARD TESTS)

To validate the findings from the Approximate Bayesian Computation (ABC) analysis (Section 3.5.1) and ensure the self-consistency of the method, we have implemented a series of "back-forward tests". These tests aim to demonstrate the ability of the posterior model parameters derived from ABC to reproduce approximately the observed $v \sin(i)$ distributions. The following are the key steps of back-forward testing:

1. Model input: Feed the spin models in each bin age with posterior distributions of B_* or χ , obtained from the ABC analysis and employ identical values for other parameters as used in the ABC procedure of Section 3.5.1.

2. Model output: Generate model-predicted $v \sin(i)$ distributions for each age bin.
3. Comparison with observations and quantifying similarity: Compare the model-generated $v \sin(i)$ distributions with the observed data and assess the similarity between distributions using the histogram intersection algorithm.

C.1. Spin models input parameters

Based on the equation 8, we developed a script that uses a set of input parameters [M_* , B_* , χ , P_{rot}^{in} , \dot{M}_{acc}^{in}] to produce the $v \sin(i)$ value for the corresponding age, as output. The analysis, consistent with the ABC approach (Section 3.5.1), is divided into two cases:

Case A: Magnetic field decreases with age

- Fixed parameters for each age bin: $M_* = 0.5M_\odot$, $\chi = 0.3$.
- Free parameters randomly chosen from specified ranges:

P_{rot}^{in} : (1, 2, 3, 4, 5, 6, 7, 8) days

\dot{M}_{acc}^{in} : Values following the probability function in Figure 3

B_* : Values following the probability function in the upper panel of Figure 17.

Case B: Branching ratio decreases with age

- Fixed parameters for each age bin: $M_* = 0.5M_\odot$, $B_* = 2000$ G.
- Free parameters randomly chosen from specified ranges:

P_{rot}^{in} and \dot{M}_{acc}^{in} : Same as case A.

χ : Values following the probability function in the lower panel of Figure 17.

For comparison purposes, we also have considered hypothetical cases, for instance, magnetic field increases with age, magnetic field remains constant with age, branching ratio increases with age, branching ratio remains constant with age, and magnetic field with branching ratio simultaneously decreases with age.

Magnetic field increases with age

- Same fixed parameters to the case A:
- Free parameters randomly chosen from specified ranges:

P_{rot}^{in} and \dot{M}_{acc}^{in} : Same as case A.

B_* : Values follow a series of Gaussian distributions with a standard deviation of 200 G and mean values [1000, 1500, 2000, 2500] G from age bin 1 to age bin 4, respectively.

Magnetic field remains constant with age

- Same fixed parameters to the case A.

B_* : follows a Gaussian distribution with a standard deviation of 200 G and a mean value of 2500 G for all bin ages.

- Free parameters randomly chosen from specified ranges:

P_{rot}^{in} and \dot{M}_{acc}^{in} : Same as case A.

Branching ratio increases with age

- Same fixed parameters to the case B:
- Free parameters randomly chosen from specified ranges:

P_{rot}^{in} and \dot{M}_{acc}^{in} : Same as case A.

χ : Values follow a series of Gaussian distributions with a standard deviation of 0.05 and mean values [0.10, 0.20, 0.30, 0.50] from age bin 1 to age bin 4, respectively.

Branching ratio remains constant with age

- Same fixed parameters to the case B.

χ : follows a Gaussian distribution with a standard deviation of 0.05 and a mean value of 0.50 for all bin ages.

- Free parameters randomly chosen from specified ranges:

P_{rot}^{in} and \dot{M}_{acc}^{in} : Same as case A.

Magnetic field and branching ratio simultaneously decreases with age

- Fixed parameters for each age bin: $M_* = 0.5M_{\odot}$.

- Free parameters randomly chosen from specified ranges:

P_{rot}^{in} and \dot{M}_{acc}^{in} : Same as case A.

B_* and χ : Values following the probability function in the upper panel and lower panel of Figure 17, respectively.

C.2. Comparison with observations

For each case and each bin age, we obtain a distribution of $v \sin(i)$ generated by spin-models. As an example, we have illustrated the resulting distributions of $v \sin(i)$ generated by spin-models for the model case χ decreasing with the age at bin 3 in comparison to its observations (Left panel of Figure 18)⁴. Employing the histogram intersection algorithm (Swain & Ballard 1991), we estimate the intercepted area between the histograms, using this value as a metric for assessing the similarity between distributions. A metric of 1 indicates identical distributions, while a metric of 0 signifies no correlation. Likewise, in the right panel of Figure 18, we show the similarity index bin by bin for all considered cases (Appendix C.1). The lack of similarity observed for slow rotators is primarily attributed to the contamination of stars with masses below the mass value utilized in our models or similarly below the typical mass for the whole sample. These slower rotators in the initial $v \sin(i)$ container correspond to stars in the age bin 1. Since the size of the star, which is directly related to $v \sin(i)$, depends on the stellar mass for a given age and the mass value used in the theoretical cases is systematically greater than the mass of the observed sample in bin 1, the models do not reproduce the slower rotators in the histograms. Although smaller values of stellar mass could fill the slower rotator container, changing the values of stellar masses would not be directly comparable to the cases addressed in Section 3.5.1.

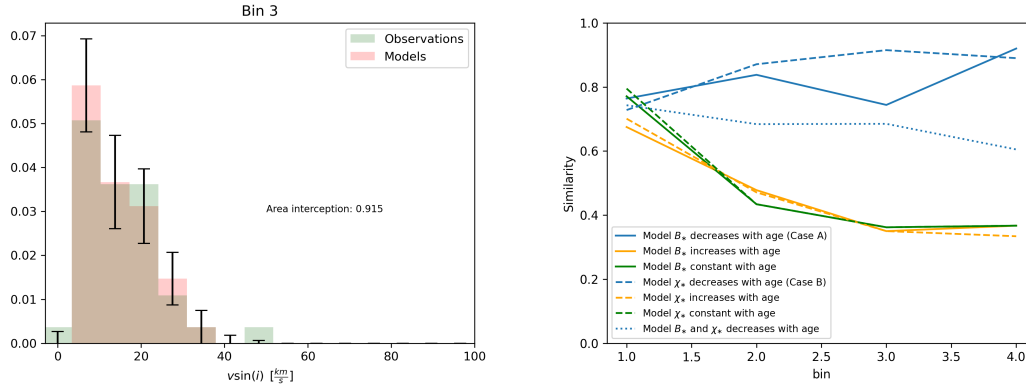


Figure 18. Similarity index between back-forward models and observations. The left panel is a comparison between observed and back-forward $v \sin(i)$ distributions. The back-forward distribution is the median of 100 runs, and the error bars represent the standard deviation. The observed $v \sin(i)$ distribution come from Figure 10. All histograms are properly normalized to the area of each distribution. The right panel shows the comparisons of all considered models.

⁴ For additional cases, we refer the reader to our GitHub repository <https://github.com/javiserna/Rotational-Evolution-of-Classical-T-Tauri-Stars-Models-and-Observations-Tests->

Finally, these tests support that the decrease of magnetic field and branching ratio with time shown in Figure 12 effectively account for $v \sin(i)$ observations of Figure 10. Validating the ABC analyses. The right panel of Figure 18, indicates to us that distributions of $v \sin(i)$ observed and predicted by the back-forward test in case A and B, tend to be similar above 80%. Also, demonstrates that a model with a magnetic field and branching ratio simultaneously decreasing with age compares better with observations than a model with these constant parameters.

REFERENCES

- Alencar, S. H. P., & Basri, G. 2000, *AJ*, 119, 1881, doi: [10.1086/301300](https://doi.org/10.1086/301300)
- Ansdell, M., Gaidos, E., Hedges, C., et al. 2019, *Monthly Notices of the Royal Astronomical Society*, 492, 572, doi: [10.1093/mnras/stz3361](https://doi.org/10.1093/mnras/stz3361)
- Armitage, P. J., & Clarke, C. J. 1996, *MNRAS*, 280, 458, doi: [10.1093/mnras/280.2.458](https://doi.org/10.1093/mnras/280.2.458)
- Artemenko, S. A., Grankin, K. N., & Petrov, P. P. 2012, *Astronomy Letters*, 38, 783, doi: [10.1134/S1063773712110011](https://doi.org/10.1134/S1063773712110011)
- Astropy Collaboration, Robitaille, T. P., Tollerud, E. J., et al. 2013, *A&A*, 558, A33, doi: [10.1051/0004-6361/201322068](https://doi.org/10.1051/0004-6361/201322068)
- Banzatti, A., Pascucci, I., Edwards, S., et al. 2019, *ApJ*, 870, 76, doi: [10.3847/1538-4357/aaf1aa](https://doi.org/10.3847/1538-4357/aaf1aa)
- Baraffe, I., Homeier, D., Allard, F., & Chabrier, G. 2015, *A&A*, 577, A42, doi: [10.1051/0004-6361/201425481](https://doi.org/10.1051/0004-6361/201425481)
- Bayo, A., Barrado, D., Huéramo, N., et al. 2012, *A&A*, 547, A80, doi: [10.1051/0004-6361/201219374](https://doi.org/10.1051/0004-6361/201219374)
- Bouvier, J., Cabrit, S., Fernandez, M., Martin, E. L., & Matthews, J. M. 1993, *A&A*, 272, 176
- Brasseur, C. E., Phillip, C., Fleming, S. W., Mullally, S. E., & White, R. L. 2019, *Astrocut: Tools for creating cutouts of TESS images*. <http://ascl.net/1905.007>
- Briceño, C., Calvet, N., Hernández, J., et al. 2019, *The Astronomical Journal*, 157, 85, doi: [10.3847/1538-3881/aaf79b](https://doi.org/10.3847/1538-3881/aaf79b)
- Cabrit, S., Edwards, S., Strom, S. E., & Strom, K. M. 1990, *ApJ*, 354, 687, doi: [10.1086/168725](https://doi.org/10.1086/168725)
- Cao, L., & Pinsonneault, M. H. 2022, *MNRAS*, 517, 2165, doi: [10.1093/mnras/stac270610.48550/arXiv.2209.10549](https://doi.org/10.1093/mnras/stac270610.48550/arXiv.2209.10549)
- Carpenter, J. M., Mamajek, E. E., Hillenbrand, L. A., & Meyer, M. R. 2006, *The Astrophysical Journal*, 651, L49, doi: [10.1086/509121](https://doi.org/10.1086/509121)
- Chandrasekhar, S., & Münch, G. 1950, *ApJ*, 111, 142, doi: [10.1086/145245](https://doi.org/10.1086/145245)
- Cody, A. M., & Hillenbrand, L. A. 2010, *Astrophys. J. Suppl. Ser.*, 191, 389, doi: [10.1088/0067-0049/191/2/389](https://doi.org/10.1088/0067-0049/191/2/389)
- Cody, A. M., Stauffer, J., Baglin, A., et al. 2014, *AJ*, 147, 82, doi: [10.1088/0004-6256/147/4/82](https://doi.org/10.1088/0004-6256/147/4/82)
- Collier Cameron, A., & Campbell, C. G. 1993a, *A&A*, 274, 309
- . 1993b, *A&A*, 274, 309
- Cranmer, S. R. 2008, *The Astrophysical Journal*, 689, 316, doi: [10.1086/592566](https://doi.org/10.1086/592566)
- Czesla, S., Schröter, S., Schneider, C. P., et al. 2019, *PyA: Python astronomy-related packages*. <http://ascl.net/1906.010>
- Donati, J. F., & Landstreet, J. D. 2009, *ARA&A*, 47, 333, doi: [10.1146/annurev-astro-082708-101833](https://doi.org/10.1146/annurev-astro-082708-101833)
- Dotter, A. 2016, *ApJS*, 222, 8, doi: [10.3847/0067-0049/222/1/8](https://doi.org/10.3847/0067-0049/222/1/8)
- Edwards, S., Fischer, W., Kwan, J., Hillenbrand, L., & Dupree, A. K. 2003, *ApJL*, 599, L41, doi: [10.1086/381077](https://doi.org/10.1086/381077)
- Emeriau-Viard, C., & Brun, A. S. 2017, *The Astrophysical Journal*, 846, 8, doi: [10.3847/1538-4357/aa7b33](https://doi.org/10.3847/1538-4357/aa7b33)
- Ercolano, B., Picogna, G., Monsch, K., Drake, J. J., & Preibisch, T. 2021, *MNRAS*, 508, 1675, doi: [10.1093/mnras/stab259010.48550/arXiv.2109.04113](https://doi.org/10.1093/mnras/stab259010.48550/arXiv.2109.04113)
- Espaillet, C. C., Robinson, C. E., Romanova, M. M., et al. 2021, *Nature*, 597, 41, doi: [10.1038/s41586-021-03751-5](https://doi.org/10.1038/s41586-021-03751-5)
- Finley, A. J., & Matt, S. P. 2017, *The Astrophysical Journal*, 845, 46, doi: [10.3847/1538-4357/aa7fb9](https://doi.org/10.3847/1538-4357/aa7fb9)
- Folsom, C. P., Petit, P., Bouvier, J., et al. 2016, *Monthly Notices of the Royal Astronomical Society*, 457, 580, doi: [10.1093/mnras/stv2924](https://doi.org/10.1093/mnras/stv2924)
- Gaia Collaboration, Vallenari, A., Brown, A. G. A., et al. 2022, *arXiv e-prints*, arXiv:2208.00211. <https://arxiv.org/abs/2208.00211>
- Gallet, F., & Bouvier, J. 2013, *Astron. Astrophys.*, 556, A36, doi: [10.1051/0004-6361/201321302](https://doi.org/10.1051/0004-6361/201321302)
- . 2015, *A&A*, 577, A98, doi: [10.1051/0004-6361/201525660](https://doi.org/10.1051/0004-6361/201525660)
- Gallet, F., Zanni, C., & Amard, L. 2019, *A&A*, 632, A6, doi: [10.1051/0004-6361/201935432](https://doi.org/10.1051/0004-6361/201935432)
- Garraffo, C., Drake, J. J., & Cohen, O. 2015, *The Astrophysical Journal*, 807, L6, doi: [10.1088/2041-8205/807/1/6](https://doi.org/10.1088/2041-8205/807/1/6)
- Gehrig, L., Steiner, D., Vorobyov, E., & Güdel, M. 2022, *arXiv e-prints*, arXiv:2208.08852. <https://arxiv.org/abs/2208.08852>
- Ghosh, P., & Lamb, F. K. 1978, *ApJL*, 223, L83, doi: [10.1086/182734](https://doi.org/10.1086/182734)
- . 1979, *ApJ*, 234, 296, doi: [10.1086/157498](https://doi.org/10.1086/157498)
- Gonneau, A., Lyubenova, M., Lançon, A., et al. 2020, *A&A*, 634, A133, doi: [10.1051/0004-6361/201936825](https://doi.org/10.1051/0004-6361/201936825)
- Gullbring, E., Hartmann, L., Briceño, C., & Calvet, N. 1998, *ApJ*, 492, 323, doi: [10.1086/305032](https://doi.org/10.1086/305032)
- Harris, C. R., Millman, K. J., van der Walt, S. J., et al. 2020, *Nature*, 585, 357, doi: [10.1038/s41586-020-2649-2](https://doi.org/10.1038/s41586-020-2649-2)
- Hartigan, P., Edwards, S., & Ghandour, L. 1995, *ApJ*, 452, 736, doi: [10.1086/176344](https://doi.org/10.1086/176344)
- Hartmann, L., Avrett, E., & Edwards, S. 1982, *ApJ*, 261, 279, doi: [10.1086/160339](https://doi.org/10.1086/160339)
- Hartmann, L., Herczeg, G., & Calvet, N. 2016, *Annual Review of Astronomy and Astrophysics*, 54, 135, doi: [10.1146/annurev-astro-081915-023347](https://doi.org/10.1146/annurev-astro-081915-023347)

- Hartmann, L., & Stauffer, J. R. 1989, *AJ*, 97, 873, doi: [10.1086/115033](https://doi.org/10.1086/115033)
- Herbst, Bailer-Jones, C. A. L., Mundt, R., Meisenheimer, K., & Wackermann, R. 2002, *A&A*, 396, 513, doi: [10.1051/0004-6361:20021362](https://doi.org/10.1051/0004-6361:20021362)
- Herczeg, G. J., & Hillenbrand, L. A. 2008, *ApJ*, 681, 594, doi: [10.1086/586728](https://doi.org/10.1086/586728)
- Hernández, J., Hartmann, L., Calvet, N., et al. 2008, *ApJ*, 686, 1195, doi: [10.1086/591224](https://doi.org/10.1086/591224)
- Hernández, J., Calvet, N., Perez, A., et al. 2014, *The Astrophysical Journal*, 794, 36, doi: [10.1088/0004-637x/794/1/36](https://doi.org/10.1088/0004-637x/794/1/36)
- Hunter, J. D. 2007, *Computing in Science & Engineering*, 9, 90, doi: [10.1109/MCSE.2007.55](https://doi.org/10.1109/MCSE.2007.55)
- Husser, T. O., Wende-von Berg, S., Dreizler, S., et al. 2013, *A&A*, 553, A6, doi: [10.1051/0004-6361/201219058](https://doi.org/10.1051/0004-6361/201219058)
- Iben, Icko, J. 1965, *ApJ*, 141, 993, doi: [10.1086/148193](https://doi.org/10.1086/148193)
- Ingleby, L., Calvet, N., Herczeg, G., et al. 2013, *The Astrophysical Journal*, 767, 112, doi: [10.1088/0004-637x/767/2/112](https://doi.org/10.1088/0004-637x/767/2/112)
- Ireland, L. G., Zanni, C., Matt, S. P., & Pantolmos, G. 2020, *The Astrophysical Journal*, 906, 4, doi: [10.3847/1538-4357/abc828](https://doi.org/10.3847/1538-4357/abc828)
- Jayawardhana, R., Coffey, J., Scholz, A., Brandeker, A., & van Kerkwijk, M. H. 2006, *The Astrophysical Journal*, 648, 1206, doi: [10.1086/506171](https://doi.org/10.1086/506171)
- Johns-Krull, C. M. 2007, *The Astrophysical Journal*, 664, 975, doi: [10.1086/519017](https://doi.org/10.1086/519017)
- Kausch, W., Noll, S., Smette, A., et al. 2015, *A&A*, 576, A78, doi: [10.1051/0004-6361/201423909](https://doi.org/10.1051/0004-6361/201423909)
- Koenigl, A. 1991, *ApJL*, 370, L39, doi: [10.1086/185972](https://doi.org/10.1086/185972)
- Kounkel, M., Covey, K., Suárez, G., et al. 2018, *The Astronomical Journal*, 156, 84, doi: [10.3847/1538-3881/aad1f1](https://doi.org/10.3847/1538-3881/aad1f1)
- Kounkel, M., Covey, K., Moe, M., et al. 2019, *AJ*, 157, 196, doi: [10.3847/1538-3881/ab13b1](https://doi.org/10.3847/1538-3881/ab13b1)
- Kounkel, M., Covey, K. R., Stassun, K. G., et al. 2021, *The Astronomical Journal*, 162, 184, doi: [10.3847/1538-3881/ac1798](https://doi.org/10.3847/1538-3881/ac1798)
- Kounkel, M., Zari, E., Covey, K., et al. 2023, arXiv e-prints, arXiv:2301.07186, doi: [10.48550/arXiv.2301.07186](https://doi.org/10.48550/arXiv.2301.07186)
- Kuhi, L. V. 1964, *ApJ*, 140, 1409, doi: [10.1086/148047](https://doi.org/10.1086/148047)
- Kurosawa, R., & Romanova, M. M. 2013, *MNRAS*, 431, 2673, doi: [10.1093/mnras/stt365](https://doi.org/10.1093/mnras/stt365)
- Lavail, A., Kochukhov, O., & Hussain, G. A. J. 2019, *A&A*, 630, A99, doi: [10.1051/0004-6361/201935695](https://doi.org/10.1051/0004-6361/201935695)
- Lavail, A., Kochukhov, O., Hussain, G. A. J., et al. 2017, *A&A*, 608, A77, doi: [10.1051/0004-6361/201731889](https://doi.org/10.1051/0004-6361/201731889)
- Lindgren, L., Klioner, S. A., Hernández, J., et al. 2020, arXiv e-prints, arXiv:2012.03380, <https://arxiv.org/abs/2012.03380>
- Lindgren, L., Bastian, U., Biermann, M., et al. 2021, *A&A*, 649, A4, doi: [10.1051/0004-6361/202039653](https://doi.org/10.1051/0004-6361/202039653)
- Liu, C., Fu, J., Shi, J., et al. 2020, arXiv e-prints, arXiv:2005.07210, <https://arxiv.org/abs/2005.07210>
- Lomb, N. R. 1976, *Ap&SS*, 39, 447, doi: [10.1007/BF00648343](https://doi.org/10.1007/BF00648343)
- Luo, A.-L., Zhao, Y.-H., Zhao, G., et al. 2015, *Research in Astronomy and Astrophysics*, 15, 1095, doi: [10.1088/1674-4527/15/8/002](https://doi.org/10.1088/1674-4527/15/8/002)
- MacGregor, K. B., & Brenner, M. 1991, *ApJ*, 376, 204, doi: [10.1086/170269](https://doi.org/10.1086/170269)
- Majewski, S. R., Schiavon, R. P., Frinchaboy, P. M., et al. 2017, *AJ*, 154, 94, doi: [10.3847/1538-3881/aa784d](https://doi.org/10.3847/1538-3881/aa784d)
- Manzo-Martínez, E., Calvet, N., Hernández, J., et al. 2020, *ApJ*, 893, 56, doi: [10.3847/1538-4357/ab7ead](https://doi.org/10.3847/1538-4357/ab7ead)
- Marjoram, P., Hamblin, S., & Foley, B. 2015, in *Proceedings of the Conference on Summer Computer Simulation, SummerSim '15* (San Diego, CA, USA: Society for Computer Simulation International), 1–8
- Matt, S., & Pudritz, R. E. 2005a, *MNRAS*, 356, 167, doi: [10.1111/j.1365-2966.2004.08431.x](https://doi.org/10.1111/j.1365-2966.2004.08431.x)
- . 2005b, *ApJL*, 632, L135, doi: [10.1086/498066](https://doi.org/10.1086/498066)
- Matt, S., & Pudritz, R. E. 2005, *The Astrophysical Journal*, 632, L135, doi: [10.1086/498066](https://doi.org/10.1086/498066)
- Matt, S., & Pudritz, R. E. 2008a, *ApJ*, 681, 391, doi: [10.1086/587453](https://doi.org/10.1086/587453)
- . 2008b, *ApJ*, 678, 1109, doi: [10.1086/533428](https://doi.org/10.1086/533428)
- Matt, S. P., Pinzón, G., de la Reza, R., & Greene, T. P. 2010, *ApJ*, 714, 989, doi: [10.1088/0004-637X/714/2/989](https://doi.org/10.1088/0004-637X/714/2/989)
- Matt, S. P., Pinzón, G., Greene, T. P., & Pudritz, R. E. 2012, *ApJ*, 745, 101, doi: [10.1088/0004-637X/745/1/101](https://doi.org/10.1088/0004-637X/745/1/101)
- Natta, A., Testi, L., Alcalá, J. M., et al. 2014, *A&A*, 569, A5, doi: [10.1051/0004-6361/201424136](https://doi.org/10.1051/0004-6361/201424136)
- Nguyen, D. C., Jayawardhana, R., van Kerkwijk, M. H., et al. 2009, *The Astrophysical Journal*, 695, 1648, doi: [10.1088/0004-637x/695/2/1648](https://doi.org/10.1088/0004-637x/695/2/1648)
- Olney, R., Kounkel, M., Schillinger, C., et al. 2020, *AJ*, 159, 182, doi: [10.3847/1538-3881/ab7a97](https://doi.org/10.3847/1538-3881/ab7a97)
- Pantolmos, G., Zanni, C., & Bouvier, J. 2020, *A&A*, 643, A129, doi: [10.1051/0004-6361/202038569](https://doi.org/10.1051/0004-6361/202038569)
- Pascucci, I., Cabrit, S., Edwards, S., et al. 2022, arXiv e-prints, arXiv:2203.10068, <https://arxiv.org/abs/2203.10068>
- Pecaut, M. J., & Mamajek, E. E. 2013, *ApJS*, 208, 9, doi: [10.1088/0067-0049/208/1/9](https://doi.org/10.1088/0067-0049/208/1/9)

- Pinzón, G., Hernández, J., Serna, J., et al. 2021, *The Astronomical Journal*, 162, 90, doi: [10.3847/1538-3881/ac04ae](https://doi.org/10.3847/1538-3881/ac04ae)
- Réville, V., Brun, A. S., Matt, S. P., Strugarek, A., & Pinto, R. F. 2015, *The Astrophysical Journal*, 798, 116, doi: [10.1088/0004-637x/798/2/116](https://doi.org/10.1088/0004-637x/798/2/116)
- Roggero, N., Bouvier, J., Rebull, L. M., & Cody, A. M. 2021, *A&A*, 651, A44, doi: [10.1051/0004-6361/202140646](https://doi.org/10.1051/0004-6361/202140646)
- Scargle, J. D. 1982, *ApJ*, 263, 835, doi: [10.1086/160554](https://doi.org/10.1086/160554)
- Schatzman, E. 1962, *Annales d'Astrophysique*, 25, 18
- Scott, D. W. 1979, *Biometrika*, 66, 605, doi: [10.1093/biomet/66.3.605](https://doi.org/10.1093/biomet/66.3.605)
- Serna, J., Hernandez, J., Kounkel, M., et al. 2021, *ApJ*, 923, 177, doi: [10.3847/1538-4357/ac300a](https://doi.org/10.3847/1538-4357/ac300a)
- Shu, F. H., Lizano, S., Ruden, S. P., & Najita, J. 1988, *ApJL*, 328, L19, doi: [10.1086/185152](https://doi.org/10.1086/185152)
- Simon, M. N., Pascucci, I., Edwards, S., et al. 2016, *ApJ*, 831, 169, doi: [10.3847/0004-637X/831/2/169](https://doi.org/10.3847/0004-637X/831/2/169)
- Smette, A., Sana, H., Noll, S., et al. 2015, *A&A*, 576, A77, doi: [10.1051/0004-6361/201423932](https://doi.org/10.1051/0004-6361/201423932)
- Somers, G., Cao, L., & Pinsonneault, M. H. 2020, *ApJ*, 891, 29, doi: [10.3847/1538-4357/ab722e](https://doi.org/10.3847/1538-4357/ab722e)
- Stassun, K. G., & Torres, G. 2021, *ApJL*, 907, L33, doi: [10.3847/2041-8213/abdaad](https://doi.org/10.3847/2041-8213/abdaad)
- Still, M., & Barclay, T. 2012, *PyKE: Reduction and analysis of Kepler Simple Aperture Photometry data*. <http://ascl.net/1208.004>
- Strugarek, A., Brun, A. S., Matt, S. P., & Réville, V. 2015, *The Astrophysical Journal*, 815, 111, doi: [10.1088/0004-637x/815/2/111](https://doi.org/10.1088/0004-637x/815/2/111)
- Swain, M. J., & Ballard, D. H. 1991, *International Journal of Computer Vision*, 7, 11. <https://api.semanticscholar.org/CorpusID:8167136>
- Thanathibodee, T., Calvet, N., Hernández, J., Maucó, K., & Briceño, C. 2022, *AJ*, 163, 74, doi: [10.3847/1538-3881/ac3ee6](https://doi.org/10.3847/1538-3881/ac3ee6)
- Tokovinin, A., Petr-Gotzens, M. G., & Briceño, C. 2020, *The Astronomical Journal*, 160, 268, doi: [10.3847/1538-3881/abc2d6](https://doi.org/10.3847/1538-3881/abc2d6)
- Tout, C. A., & Pringle, J. E. 1992, *MNRAS*, 256, 269, doi: [10.1093/mnras/256.2.269](https://doi.org/10.1093/mnras/256.2.269)
- Turner, B. M., & Van Zandt, T. 2012, *Journal of Mathematical Psychology*, 56, 69, doi: <https://doi.org/10.1016/j.jmp.2012.02.005>
- Uzdensky, D. A. 2004, *Ap&SS*, 292, 573, doi: [10.1023/B:ASTR.0000045064.93078.87](https://doi.org/10.1023/B:ASTR.0000045064.93078.87)
- Vernet, J., Dekker, H., D'Odorico, S., et al. 2011, *A&A*, 536, A105, doi: [10.1051/0004-6361/201117752](https://doi.org/10.1051/0004-6361/201117752)
- Vidotto, A. A., Gregory, S. G., Jardine, M., et al. 2014, *Monthly Notices of the Royal Astronomical Society*, 441, 2361, doi: [10.1093/mnras/stu728](https://doi.org/10.1093/mnras/stu728)
- Watson, D. M., Calvet, N. P., Fischer, W. J., et al. 2016, *The Astrophysical Journal*, 828, 52, doi: [10.3847/0004-637x/828/1/52](https://doi.org/10.3847/0004-637x/828/1/52)
- Weber, E. J., & Davis, Leverett, J. 1967, *ApJ*, 148, 217, doi: [10.1086/149138](https://doi.org/10.1086/149138)
- Yi, I. 1994, *ApJ*, 428, 760, doi: [10.1086/174283](https://doi.org/10.1086/174283)
- Zanni, C., & Ferreira, J. 2013, *A&A*, 550, A99, doi: [10.1051/0004-6361/201220168](https://doi.org/10.1051/0004-6361/201220168)